Article

Developmental Cell

ER-Golgi-localized proteins TMED2 and TMED10 control the formation of plasma membrane lipid nanodomains

Graphical abstract

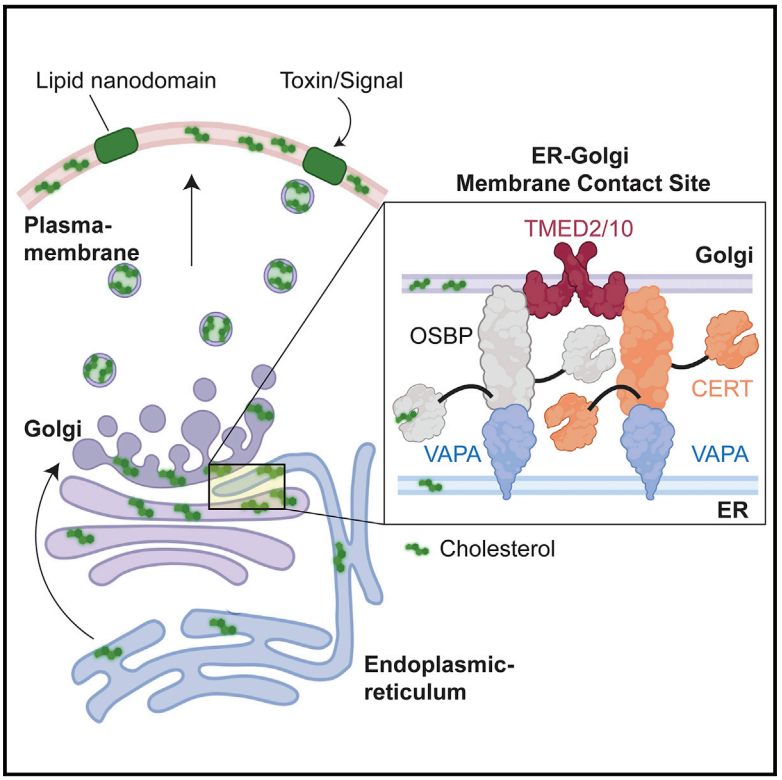

Authors

Muhammad U. Anwar,
Oksana A. Sergeeva,
Laurence Abrami, ..., Prisca Liberali,
Giovanni D'Angelo,
F. Gisou van der Goot

Correspondence

giovanni.dangelo@epfl.ch (G.D.),
gisou.vandergoot@epfl.ch (F.G.v.d.G.)

In brief

Anwar et al. show that organization of the plasma membrane into nanodomains, which are required for anthrax intoxication, depends on the transfer of cholesterol at sites where the endoplasmic reticulum and the Golgi contact each other. This transfer depends on a protein supercomplex that is organized by two proteins, TMED2 and TMED10.

Highlights

- Anthrax intoxication requires the p24 protein family members TMED2 and TMED10
- TMEDs maintain lipid transfer protein complexes at endoplasmic reticulum (ER)-Golgi membrane contacts
- ER-Golgi MCSs control cell-surface lipid nanodomain formation

Anwar et al., 2022, Developmental Cell *57*, 2334–2346
October 10, 2022
https://doi.org/10.1016/j.devcel.2022.09.004

CellPress

CellPress
OPEN ACCESS

Developmental Cell

Article

ER-Golgi-localized proteins TMED2 and TMED10 control the formation of plasma membrane lipid nanodomains

Muhammad U. Anwar,[1,5] Oksana A. Sergeeva,[1,5] Laurence Abrami,[1,5] Francisco S. Mesquita,[1] Ilya Lukonin,[3,4] Triana Amen,[1] Audrey Chuat,[1] Laura Capolupo,[2] Prisca Liberali,[3,4] Giovanni D'Angelo,[2,*] and F. Gisou van der Goot[1,6,*]

[1]Global Health Institute, School of Life Sciences, EPFL, 1015 Lausanne, Switzerland
[2]Institute of Bioengineering, School of Life Sciences, EPFL, 1015 Lausanne, Switzerland
[3]Friedrich Miescher Institute for Biomedical Research (FMI), 4058 Basel, Switzerland
[4]University of Basel, 4056 Basel, Switzerland
[5]These authors contributed equally
[6]Lead contact
*Correspondence: giovanni.dangelo@epfl.ch (G.D.), gisou.vandergoot@epfl.ch (F.G.v.d.G.)
https://doi.org/10.1016/j.devcel.2022.09.004

SUMMARY

To promote infections, pathogens exploit host cell machineries such as structural elements of the plasma membrane. Studying these interactions and identifying molecular players are ideal for gaining insights into the fundamental biology of the host cell. Here, we used the anthrax toxin to screen a library of 1,500 regulatory, cell-surface, and membrane trafficking genes for their involvement in the intoxication process. We found that endoplasmic reticulum (ER)-Golgi-localized proteins TMED2 and TMED10 are required for toxin oligomerization at the plasma membrane of human cells, an essential step dependent on localization to cholesterol-rich lipid nanodomains. Biochemical, morphological, and mechanistic analyses showed that TMED2 and TMED10 are essential components of a supercomplex that operates the exchange of both cholesterol and ceramides at ER-Golgi membrane contact sites. Overall, this study of anthrax intoxication led to the discovery that lipid compositional remodeling at ER-Golgi interfaces fully controls the formation of functional membrane nanodomains at the cell surface.

INTRODUCTION

Pathogens have evolved to co-opt existing cellular processes of their hosts. Consequently, studies of host-pathogen interactions are continuously deepening our understanding of fundamental biological processes and have helped uncover ones such as the fusion of synaptic vesicles, dynamics of the actin cytoskeleton, or retrograde transport from the Golgi to the endoplasmic reticulum (ER) (Mañes et al., 2003; Mesquita et al., 2020; Schiavo and van der Goot, 2001). Here, we searched for genes enabling anthrax intoxication, which uncovered proteins involved in the compartmentalization of the plasma membrane.

Anthrax toxin is an exotoxin secreted by virulent strains of *Bacillus anthracis* and composed of three polypeptides; two enzymatic subunits, lethal factor (LF) and edema factor (EF); and one receptor binding subunit, protective antigen (PA). During the intoxication process (Figure 1A), the monomeric 83-kDa precursor of PA (PA^{83}) first binds to one of two toxin receptors, CMG2 or TEM8, at the cell surface (Friebe et al., 2016). PA^{83} is then cleaved by proprotein convertases, such as furin (Klimpel et al., 1992; Sergeeva and van der Goot, 2019). This process is enhanced when the receptor-bound PA and the protease are brought together through association with cholesterol-rich nanodomains (Abrami et al., 2003; Levental et al., 2020).

The cleaved 63-kDa PA (PA^{63}) oligomerizes into a ring-like structure (PA^{oligo}) (Milne et al., 1994) that binds the enzymatic subunits LF and EF (Friebe et al., 2016). The hetero-oligomeric toxin-receptor complex is then internalized and trafficked to late endosomes (Abrami et al., 2004, 2006, 2010a, 2010b; Figure 1A) where the acidic environment triggers membrane insertion of the PA oligomer. This forms a membrane translocation pore (PA^{pore}) through which EF and LF are transported (Krantz et al., 2006; Sun and Jacquez, 2016) ultimately, allowing them access to the cytosol where they exert their toxic roles: LF cleaves mitogen-activated protein kinase kinases (MAPKKs) and EF increases cyclic AMP (cAMP) levels (Friebe et al., 2016).

While a global view of the mechanism of anthrax intoxication is available, the molecular players of many steps are still unknown. We therefore undertook an image-based RNA interference (RNAi) screen to identify modulators of the toxin uptake route. Several factors affected PA cleavage and pore formation, indicating that these early steps require the action of multiple cellular proteins. Unexpectedly, downregulating two proteins in the early secretory pathway, transmembrane emp24 domain containing

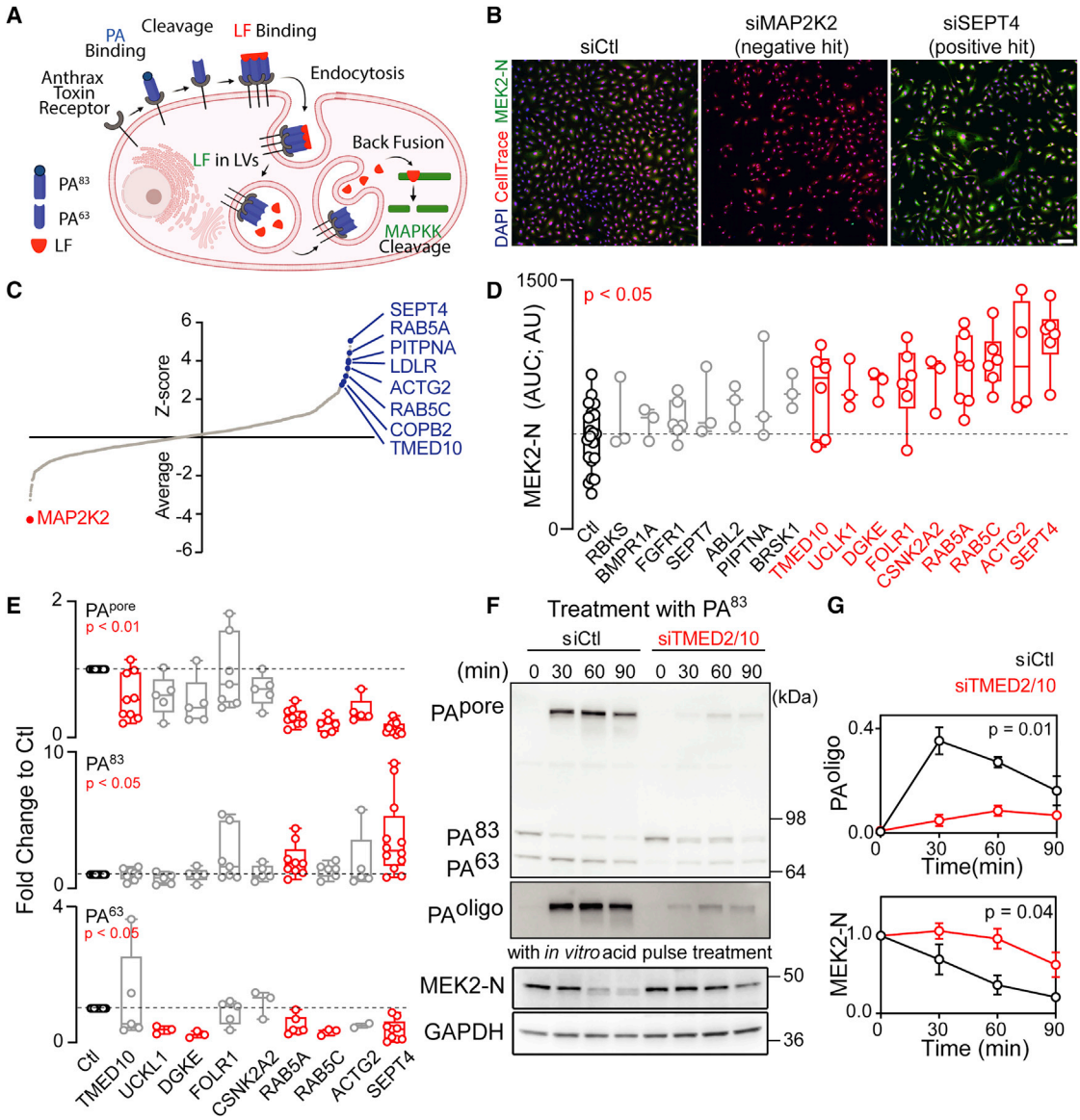

Figure 1. TMED2/10 are required for anthrax intoxication

(A) Schematic representation of anthrax intoxication.

(B) Representative IF images obtained in the image-based screen for anthrax intoxication. siSEPT4 and siMAP2K2 are examples of positive and negative hits, respectively. CellTrace, red; anti MEK2-N, green; Scale bars, 100 μm.

(C) Image-based screen results sorted by increasing *Z* score. Representative genes whose knockdown impaired MEK2 cleavage are in blue; MAP2K2 (a.k.a. MEK2) knockdown served as a specificity control (in red).

(D) Effect of the knockdown of selected hits from the screening on MEK2 cleavage as assessed by western blot in a 0–90-min intoxication time course, with each point representing the area under the curve for normalized MEK2 values. Red represents conditions where MEK2 cleavage was significantly impaired ($p < 0.05$).

(E) Effect of silencing hit genes validated in (D) on the levels of PA^{63} (lower panel), PA^{83} (middle panel), and PA^{pore} (upper panel). Red represents conditions with significant changes.

(F) Western blot of control and siTMED2/10-treated cells after anthrax toxin treatment for the indicated times. Membranes were probed with antibodies against PA, MEK2-N, and GAPDH.

(G) Quantification of PA^{oligo} rendered SDS resistant by acidification of the cell lysate (upper panel) and MEK2-N cleavage (lower panel) from the western blot for both conditions. Results are mean ± SEM (n = 3). p values are from unpaired two-tailed t test.

See also Figure S1.

protein (TMED)2 and 10, prevented PA oligomerization at the plasma membrane. Intriguingly, TMED2/10 silencing led to a loss of surface cholesterol-rich nanodomains required for the toxin's mode of action (Levental et al., 2020). In-depth analysis showed that these two proteins act as essential organizers of large protein supercomplexes at ER-Golgi membrane contact

sites (MCSs), responsible for the specific transfer of cholesterol and ceramide between the two organelles. Thus, by screening for molecular players in the anthrax intoxication process, we retrieved key components of the molecular machinery necessary for the formation of functional plasma membrane lipid domains that are relevant for pathogen infection and fundamental physiological processes.

RESULTS

TMED2/10 are required for anthrax intoxication

To identify genes involved in anthrax intoxication, we developed an image-based screen that employed the N-terminal cleavage of the MAPKK MEK2 as a readout, as MAPKKs are cleaved by LF upon productive cell intoxication (Park et al., 2002; Figure 1A). For this screen, we chose an siRNA library against 1,500 genes, which included a validated library of endocytosis and kinase genes with additional siRNAs against cell-surface proteins (Liberali et al., 2014). Cells were first silenced with siRNAs, incubated with the two anthrax toxin subunits (PA and LF), fixed, and then stained using an antibody against the N terminus of MEK2 (MEK2-N). The MEK2-N signal decreased in control cells, while remaining high when silencing genes affecting anthrax toxin entry (Figure 1B). We identified 94 silencing conditions with significantly higher MEK2-N levels than in controls (Z score > 2; Figure 1C).

Anthrax toxin utilizes multiple features of the endocytic system for its internalization and toxicity, and therefore a risk posed by the screen was the overrepresentation of genes that affect the general integrity of endosomes. To evaluate this potential bias, in addition to the staining of MEK2, cells were also stained with the early endosomal marker, early endosome antigen (EEA) 1, and the integrity of the endosomal compartment was quantified by computing the cell-number normalized perimeter of the EEA1 staining per well (see STAR Methods). By this metric we estimated the degree of fragmentation/dispersion of the endosomal compartment (Figures S1A and S1B): 85 silencing conditions had significantly altered endosomal morphology (Z score > 2 or < −2; Table S1). Interestingly, hits from the EEA1 and toxin entry screens differed largely, with only 16 silencing conditions impacting both endosomal morphology and anthrax intoxication (randomly expected common hits 5.7). This suggests that the molecular machinery assisting anthrax toxin endocytosis is distinct from that responsible for maintaining early endosome morphology (Figure 1B).

We next compared the results of the anthrax toxin entry screen to those of the endocytome screens, which tested the dependence of multiple endocytic pathways on signaling and trafficking genes (Liberali et al., 2014). The endocytome screens yielded five categories of endocytic processes that are regulated by distinct groups of genes (i.e., regulatory modules). These processes are cholera toxin B subunit (ChTxB) uptake, transferrin endocytosis, EGF endocytosis, and LDL endocytosis/micropinocytosis (Liberali et al., 2014). The associated regulatory modules can be visualized in the form of a map by computing the functional interactions (i.e., the degree of common involvement in the different endocytic processes) among the genes involved (Figure 5C in Liberali et al., 2014). We mapped the Z scores associated with the anthrax toxin entry screen onto these modules and observed that high Z score values were associated to the cluster of genes regulating EGF endocytosis (Figure S1C). In the original study (Liberali et al., 2014), EGF was used at a concentration under which EGF is endocytosed by both clathrin-dependent and -independent pathways. This similarity suggests that anthrax toxin entry has general molecular requirements similar to those of EGF endocytosis, consistent with previous findings (Abrami et al., 2003, 2004, 2006).

Based on high Z scores, detectable expression in retinal pigment epithelial (RPE1) cells, and efficient silencing by siRNA, we chose the 14 best hits for mechanistic characterization (Table S2). Anthrax toxin entry can be followed by monitoring (Figure 1A) these three steps: (1) binding of PA^{83} and its subsequent cleavage into PA^{63}, occurring at the cell surface; (2) formation of the SDS-resistant oligomeric PA^{pore}, occurring in the acidic endosomes; and (3) MEK2 cleavage, revealing the release of LF into the cytosol. All three steps were monitored using western blotting against PA or MEK2-N, either at a single time point (30 min) or as a function of time.

Silencing these 14 candidates had no effect on the surface expression of the toxin receptor CMG2 (Figures S1D and S1E), whereas silencing 9 of these reduced the kinetics of MEK2 cleavage (Figure 1D). Five candidates (ACTG2, RAB5A, RAB5C, SEPT4, and TMED10) inhibited the formation of PA^{pore}, and silencing two (SEPT4 and RAB5A) increased the amount of cell-bound PA^{83} due to diminished cleavage into PA^{63} (Figure 1E). TMED10 stood out as particularly interesting because it is reported as a protein of the early secretory pathway, yet its silencing inhibited the formation of PA^{pore} without affecting the amount of anthrax toxin receptor at the plasma membrane, nor toxin cleavage (Figures 1E, S1D, and S1E).

TMED10 belongs to a family of type I transmembrane (TM) proteins with a large domain and a short cytosolic tail (Emery et al., 2000; Gommel et al., 1999). TMED members can hetero-oligomerize, and TMED10 in particular has been shown to dimerize with TMED2 (Zavodszky and Hegde, 2019). Consistently, silencing TMED2 or TMED2 and TMED10 together inhibited LF-dependent MEK2 cleavage and the formation of PA^{pore} in endosomes (Figures 1F, 1G, S1F, and S1H). For all further studies, we therefore silenced both TMED2 and TMED10 simultaneously.

When addressing the role of TMED2 and TMED10 in pore formation, we found that PA fails to oligomerize in TMED2- and/or TMED10-depleted cells (Figures 1F, 1G, S1F, and S1G). This was determined by an *in vitro* acid pulse, where cell lysates are treated with acidic buffer to trigger the conversion of all oligomers to SDS-resistant PA^{pore}. To further confirm that TMED2/10 affect PA oligomerization, we converted PA^{83} to PA^{63} *in vitro* using trypsin prior to its addition to cells. PA^{pore} formation was still delayed (Figures S1H and S1I). Overall, these observations indicate that TMED2/10 specifically affect PA oligomerization at the cell surface.

TMED2/10 affect the formation of functional plasma membrane lipid nanodomains

PA^{63} oligomerization requires its association with detergent-resistant membranes (DRMs) (Abrami et al., 2003; Sergeeva and van der Goot, 2019). These are membranes that display resistance to solubilization at 4°C in specific detergents, such

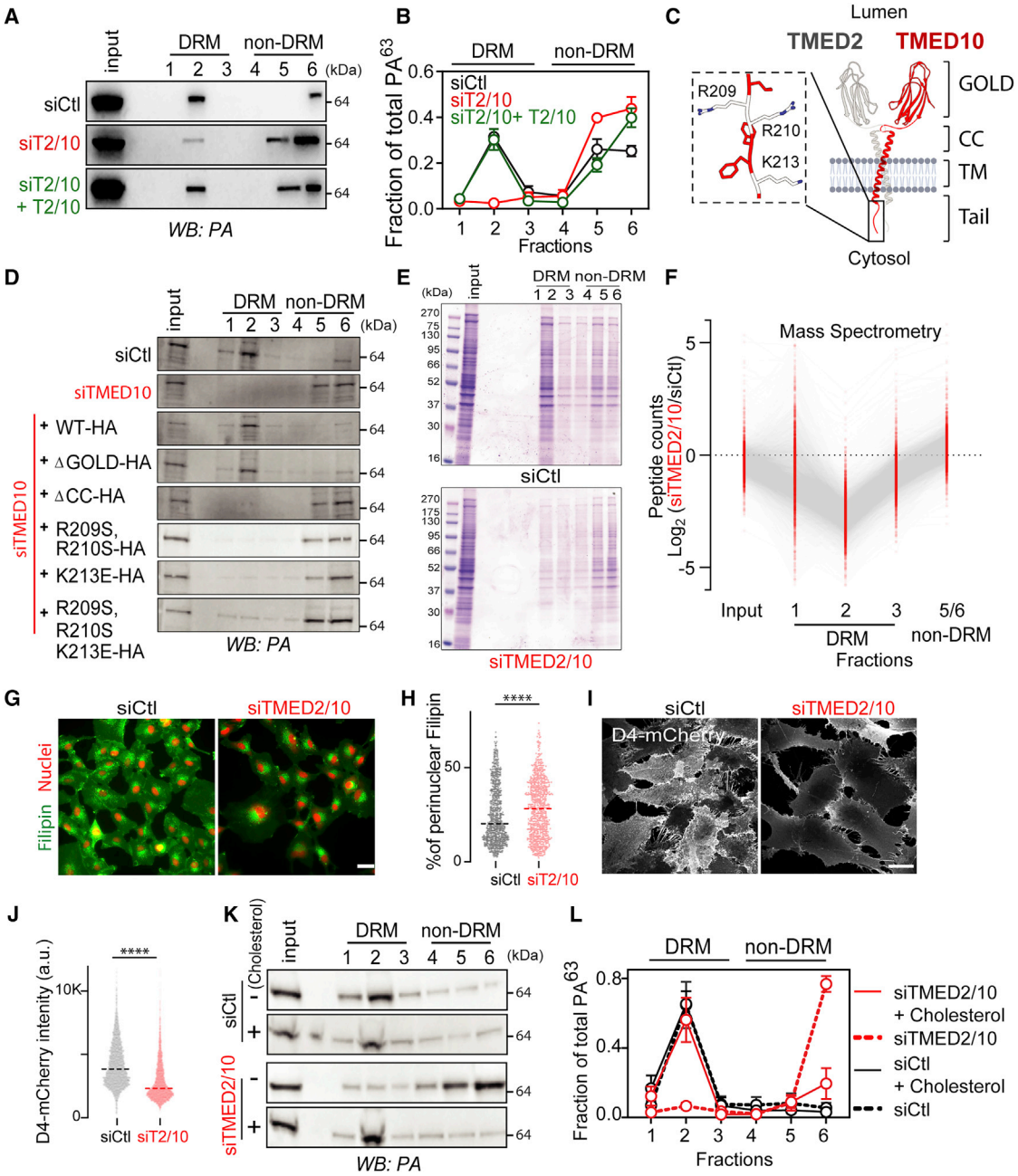

Figure 2. TMEDs are required for the assembly of lipid nanodomains

(A) Western blot of step gradient fractions from control and siTMED2/10 cells with or without TMED2/10 overexpression. Membranes were probed with anti-PA.

(B) Quantification of western blot in (A) were normalized within each experiment.

(C) Schematic representation of TMED2/10 hetero-dimer showing main domains: Golgi dynamics (GOLD), coiled coil (CC), transmembrane (TM), and cytoplasmic tail. Positively charged residues are labeled within the tail (magnified view). The lumen could be either Golgi or ER.

(D) Same as (A), with overexpression of different TMED10 mutants (see also Figure S2A).

(E) Same as in (A), fractions were run on SDS-PAGE and gels were stained with Coomassie.

(F) Same as in (A), fractions were submitted for mass spec either as fraction 1, 2, 3, or an equal combination of 5 and 6 (labeled 5/6). Each point represents the $\log_2$ ratio of one protein's abundance in siTMED2/10 over siCtl.

(G) Silenced cells were fixed and stained with filipin and NucGreen.

(H) Each cell from (G) was segmented and quantified for its total and perinuclear average integrated filipin signal intensity. The median of the proportion of the perinuclear to total filipin signal was graphed. n = 881, siCtl; n = 772, siTMED2/10 from three replicates.

(I) Control and silenced TMED2/10 cells were fixed and stained with D4-mCherry.

(legend continued on next page)

as Triton X-100. DRMs have been proposed to represent cholesterol-rich nanodomains (Levental et al., 2020). The use of detergent resistance to characterize ordered membrane domains has led to major controversy (Munro, 2003). Also, DRMs should by no means be considered equivalent to nanodomains. A variety of studies, including cross-validations, recently reviewed by Levental et al. (2020), have however rehabilitated DRMs as a useful comparative biochemical readout. In particular, it is useful to study anthrax toxin, as previous studies showed that PA^{63} association with DRMs is cholesterol dependent (Abrami et al., 2003).

We thus investigated PA^{63} association to DRMs upon TMED2/10 silencing. Strikingly, while PA^{63} was retrieved in the DRM fraction (fraction 2) of control cells as previously shown, it was solely found in the detergent-soluble fractions (5 and 6) of TMED2/10-silenced cells. This was not due to an off-target effect of the siRNA, since it could be reverted by recomplementation with siRNA-resistant TMED2 and/or TMED10 constructs (Figures 2A and 2B).

We next examined which domain of TMED10 was responsible for the recovery of PA in the DRM fraction by recomplementing siRNA-silenced cells with modified TMED10 constructs lacking specific domains (Figure 2C). Recomplementation with a construct lacking the N-terminal luminal Golgi dynamics (GOLD) domain, involved in the binding to glycosylphosphatidylinositol-anchored proteins, allowed for the recovery of DRM-associated PA. By contrast, when expressing constructs missing the coiled-coil domain, involved in dimerization of TMEDs (Zavodszky and Hegde, 2019), PA remained detergent soluble. Mutants with modifications, even single-point mutations, to the charged residues of the cytosolic tail also did not permit recovery of DRM-associated PA (Figures 2D and S2A). Thus, the abilities of TMED10 to dimerize as well as to organize interactions via its cytosolic tail (Gommel, 2001; Zavodszky and Hegde, 2019) are necessary to recover PA in the DRM fraction. By contrast, the lack of effect of the GOLD domain deletion indicates that the vesicular trafficking, cargo receptor, function of TMED2/10 does not significantly contribute to PA association with DRMs.

A decreased presence in fraction 2 of TMED2/10-silenced cells was not specific to PA; the levels of other proteins commonly found in nanodomains, such as flotillin and CMG2, also decreased significantly (Figure S2B). Global assessment of protein association to the different fractions of the gradient by Coomassie staining and mass spectrometry analysis (Figures 2E and 2F) confirmed a generalized and profound reduction in fraction 2 in TMED2/10-silenced cells. These observations suggest that TMED2/10 play a widespread role in establishing lipid domains rather than specifically affecting PA association with them. Noteworthy, in spite of this generalized effect, TMED2/10-silenced cells are viable, although they grow slower and display cell-cycle defects (Figures S2C and S2D).

Cholesterol is an indispensable component of nanodomains (Levental et al., 2020), and we have previously shown that extracting cholesterol with methyl-ß-cyclodextrin (mßCD) affects anthrax toxin action (Abrami et al., 2003). We thus investigated the effect of TMED2/10 silencing on the cellular distribution of cholesterol. We visualized cholesterol by labeling cells with the fluorescent cholesterol-binding fungal metabolite filipin III (Maxfield and Wüstner, 2012; Whitfield et al., 1955). The labeling was strikingly different in TMED2/10-silenced cells as compared with controls: instead of a marked plasma membrane staining, cholesterol accumulated in the perinuclear region (Figures 2G and 2H).

Counterstaining with organelle markers for the ER, Golgi complex, and lipid droplets showed that cholesterol accumulated partially in the Golgi region and in structures possibly representing the endo/lysosomal compartment (Figure S2E). Since filipin III binding is not only sensitive to cholesterol amounts but also to its environment (Ikonen and Zhou, 2021), we also performed staining with a second cholesterol sensor, D4-mCherry, a perfringolysin O derivative that binds accessible cholesterol (Ramachandran et al., 2002) (see STAR Methods). Staining of non-permeabilized cells with D4-mCherry was consistent with a reduced level of cholesterol at the plasma membrane (Figures 2I and 2J).

As TMED2 has been reported to bind sphingomyelin (Contreras et al., 2012), another component of nanodomains (Levental et al., 2020), and to affect sphingomyelin levels (Jiménez-Rojo et al., 2020), we tested whether the presence of sphingomyelin was reduced at the cell surface of TMED2/10-silenced cells. Labeling non-permeabilized cells with the earthworm sphingomyelin-binding toxin lysenin, however, indicated that in our conditions, surface sphingomyelin levels were not substantially different between control and silenced cells (Figure S2F).

We next tested whether the reduction in cholesterol at the plasma membrane is the main reason for the observed phenotype. Exogenous cholesterol was added by treating cells with 1 mM mßCD/cholesterol complexes (mßCD-Chol). This treatment was sufficient to recover PA in fraction 2 (Figures 2L and 2M), indicating that the reduction of surface cholesterol is the major reason for the loss of DRM-associated PA in TMED2/10-silenced cells.

TMED2 and TMED10 affect lipid fluxes through the secretory pathway

Because intracellular cholesterol distribution is altered upon TMED2/10 silencing, we wondered if this was due to a general defect in membrane transport through the secretory pathway. Although we could confirm a defect in the transport of a synchronizable glycosylphosphatidylinositol (GPI)-anchored reporter from the ER to the plasma membrane (Boncompain et al., 2012; Figure S2G), we observed no decrease in the bulk flow secretion in siTMED2/10, which was actually significantly enhanced (Figure S2H). These data, along with the evidence that the TMED GOLD domain is dispensable for the TMED-dependent PA association with DRMs, indicate that the membrane trafficking functions of TMED2/10 do not play any major role in the observed phenotypes.

We thus asked if cholesterol metabolism is compromised in siTMED2/10 cells. Lipidomics showed that cholesteryl esters (CholEs) were substantially elevated upon TMED2/10 silencing, whereas no significant changes were observed in overall

(J) Average intensity from cells in (I) of surface mCherry is plotted per cell per condition. n = 5,078, siCtl; n = 6,151, siTMED2/10 from three replicates.
(K and L) Same as in (A) and (B), the silenced cells were either untreated or nourished with cholesterol through βCD-cholesterol (1 mM) treatment for 24 h. Results are mean ± SEM (n = 3). For (G–K) *p < 0.05, ****p < 0.0001 (unpaired two-tailed t test). Scale bars, 10 μm.
See also Figure S2.

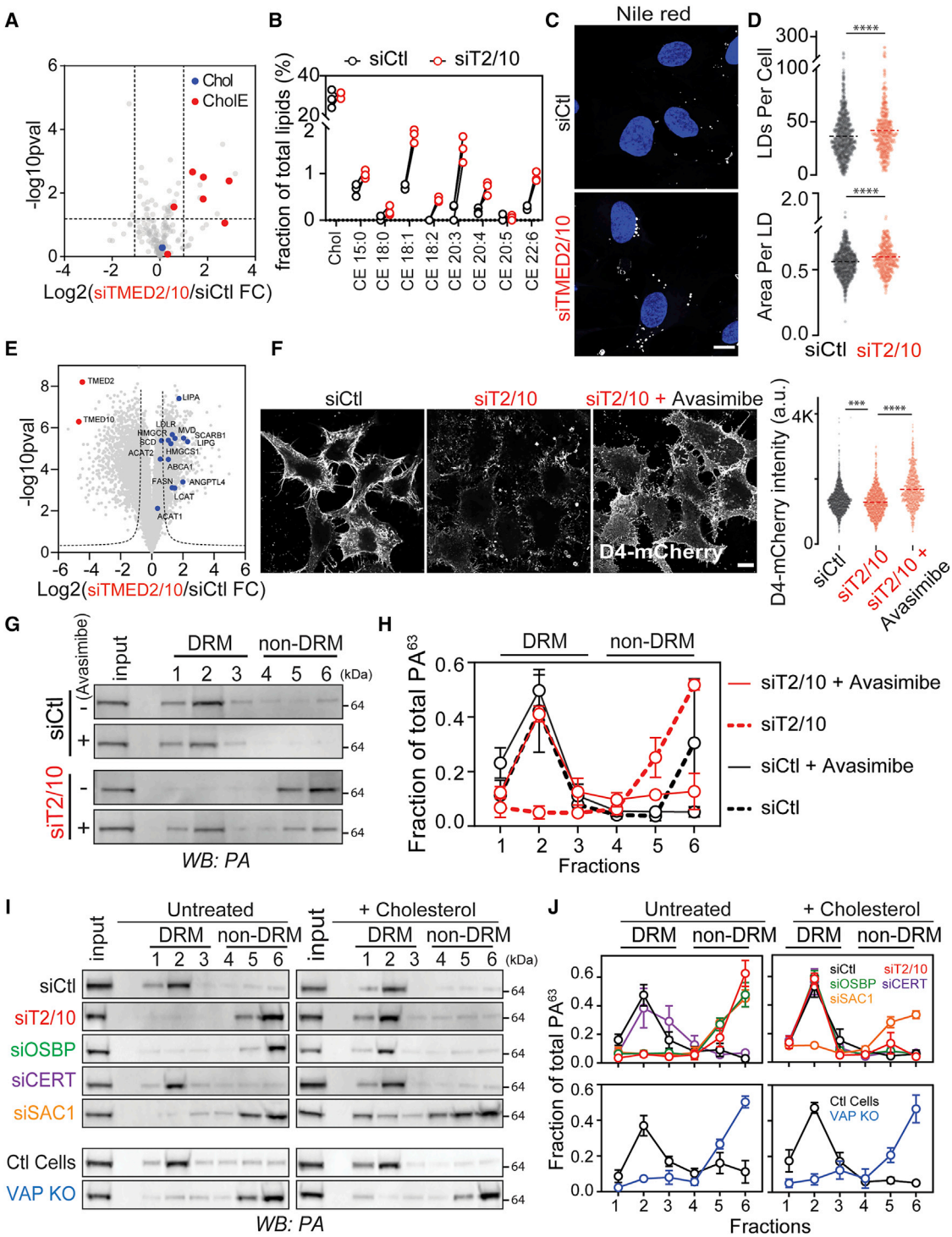

Figure 3. TMED2/10 affect cholesterol transport to the cell surface

(A) Lipidomic analysis of siCtl and siTMED2/10 cells. Data are p value versus log2FC of the siTMED2/10/ over Ctl. The cholesterol and cholesteryl esters (CholEs) are highlighted.

(B) Levels of Chol and different CholE subspecies in siCtl and siTMED2/10.

(C) Control and silenced TMED2/10 cells were fixed and stained with Hoechst (nuclei, blue) and Nile Red (LDs, gray) and imaged using laser scanning confocal microscopy.

(D) LDs in each condition were segmented based on the Nile Red signal. Average intensity and droplet size were calculated per cell in each condition. n = 1,140, siCtl; n = 449, siTMED2/10 from three replicates.

(legend continued on next page)

cholesterol levels (Figures 3A and 3B). Accordingly, the size and number of lipid droplets (where CholEs are stored) increased upon TMED2/10 silencing (Figures 3C and 3D).

RNA-seq analysis of TMED2/10-silenced cells consistently showed that acylCoA:cholesterol acyltranferases (ACATs) 1 and 2 were upregulated. In fact, various genes involved in cholesterol biosynthesis or uptake were increased, such as HMG-CoA synthase 1 (HMGCS1), HMG-CoA reductase (HMGCR), diphosphomevalonate decarboxylase (MVD), and stearoyl-CoA desaturase (SCD1) (Figure 3E). The increase could also be observed at the protein level (Figures S3A and S3B). The LDL receptor gene was also upregulated, and its subcellular localization remained unchanged in silenced cells (Figures S3C and S3D), indicating that defective cholesterol uptake is unlikely to play a role in the observed phenotypes.

As TMED2/10 silencing impacts sterol esterification, we tested whether inhibiting ACATs might restore the flux of cholesterol toward the plasma membrane. Upon ACAT inhibition, we indeed observed a recovery of plasma membrane levels of cholesterol as assessed by D4-mCherry (Figure 3F) and the concomitant DRM association of PA (Figures 3G and 3H).

We conclude that silencing TMED2/10 prevents cholesterol from reaching its normal levels at the plasma membrane and promotes its esterification and storage in lipid droplets. These effects inhibit the formation of plasma membrane lipid nanodomains and thus the oligomerization of PA.

Membrane contact site components are involved in plasma membrane nanodomain formation

Cholesterol is synthesized in the ER and is then transported to the Golgi, either in vesicles or, more substantially, via the oxysterol-binding protein (OSBP), a lipid transfer protein that localizes at MCSs between the two compartments (Mesmin et al., 2013, 2019). Once at the Golgi, cholesterol is included into membrane carriers that leave the organelle en route to the plasma membrane (Antonny et al., 2018; Luo et al., 2020).

Upon OSBP inhibition, cholesterol transport to the Golgi is diminished, undergoes esterification in the ER, and is stored in lipid droplets (Luo et al., 2020). OSBP also ensures the transport of phosphatidylinositol-4-phosphate (PtdIns(4)P) from the Golgi to the ER for its dephosphorylation, serving as a counterflow for cholesterol transfer (Antonny et al., 2018; Hanada et al., 2009). Interestingly, in TMED2/10-silenced cells, PtdIns(4)P accumulated on the Golgi phenocopying OSBP inhibition (Figures S3E and S3F).

Finally, sites of contact between ER and Golgi also mediate transfer of ceramide for its conversion to sphingomyelin. This is operated by the cytosolic ceramide transporter (CERT) (Hanada et al., 2009). Upon TMED2/10 silencing, ceramide conversion to sphingomyelin was impaired, and glucosylceramide synthesis and steady-state levels were strongly increased (Figures S3G and S3H), phenocopying CERT inhibition (Capasso et al., 2017; Hanada et al., 2003, 2009).

The high level of esterified cholesterol, the Golgi accumulation of PtdIns(4)P, and reduced sphingomyelin production in TMED2/10-silenced cells raised the hypothesis that these proteins play a key role in lipid exchange at MCSs between the ER and the Golgi, two compartments between which they are known to cycle (Strating and Martens, 2009). This hypothesis predicts that established MCS components (Venditti et al., 2019), when silenced, should similarly affect the recovery of PA in DRM fractions as silencing TMED2/10. OSBP association with the ER is mediated by the dimeric TM VAMP associated protein (VAP) A, while its association with the Golgi occurs through ADP ribosylation factor (ARF) 1 and PtdIns(4)P (Antonny et al., 2018; Levine and Munro, 2002; Mesmin et al., 2013). The PtdIns(4)P phosphatase, also known as suppressor of Actin mutations 1-like protein (SAC1), which ensures that the phosphoinositide is consumed when transported to the ER (Mesmin et al., 2019), is also a key player of MCSs, since PtdIns(4)P has been proposed to be the energy source in the transport of cholesterol against its concentration gradient. Silencing SAC1 and OSBP, but not CERT, led to a loss of DRM-associated PA. The phenotype of OSBP silencing could again be reverted by the exogenous addition of cholesterol (Figures 3I and 3J).

To study the role of VAPs, we used an available double knockout cell line for VAPA and VAPB (Dong et al., 2016). In these cells, PA was lost from fraction 2, and this association could only be moderately recovered by cholesterol addition (Figures 3I and 3J). Consistently, D4 staining showed that surface cholesterol levels were significantly reduced in VAPA/B knockout cells (Figures S3I and S3J). Differently from siTMED2/10 cells, VAPA/B knockout cells showed a substantial decrease in plasma membrane sphingomyelin, as assessed by lysenin staining (Figure S3K). The lack of DRM recovery suggests that cholesterol, in the absence of sphingolipids, is insufficient for the formation of surface nanodomains. VAPA/B knockout cells also differed from TMED2/10-silenced cells in that ACATs and SCD1 were not upregulated (Figures S3L and S3M).

From the plasma membrane, cholesterol can be endocytosed and recycled through a RAB11-dependent pathway to the Golgi and then back to the plasma membrane (Ikonen and Zhou, 2021). Importantly, disrupting cholesterol recycling from endosomes by silencing RAB11 or the general endosomal regulator RAB4 (McCaffrey et al., 2001; Takahashi et al., 2007) had no effect on DRM association of PA (Figures S4A and S4B), suggesting that nanodomain formation mainly relies on MCS components involved in cholesterol transfer between the ER and the Golgi, i.e., VAPA/B, OSBP, and SAC1.

(E) RNA-seq analysis of siTMED2/10 versus siCtl cells. Genes involved in cholesterol transport and synthesis are highlighted in blue. Data are −10logpval versus log2FC of the siTMED2/10 over siCtl ratio.
(F) HeLa control and TMED2/10-silenced cells were fixed and stained for D4-mCherry. Cells were either treated with avasimibe (10 μM) or not (Ctrl). Average intensity of surface mCherry from the images is plotted per cell per condition. n = 1,676, siCtl; n = 1,102, siTMED2/10; n = 786, siTMED2/10 + avasimibe from three replicates.
(G) Western blot of step-gradient fractions in control and siTMED2/10 cells with or without avasimibe treatment. Membranes were probed with anti-PA.
(H) The values from (G) were normalized within each experiment.
(I and J). Same as in (G) and (H), silenced cells were either treated or not with mβCD-Chol (1 mM). Scale bars, 10 μm.
See also Figure S3.

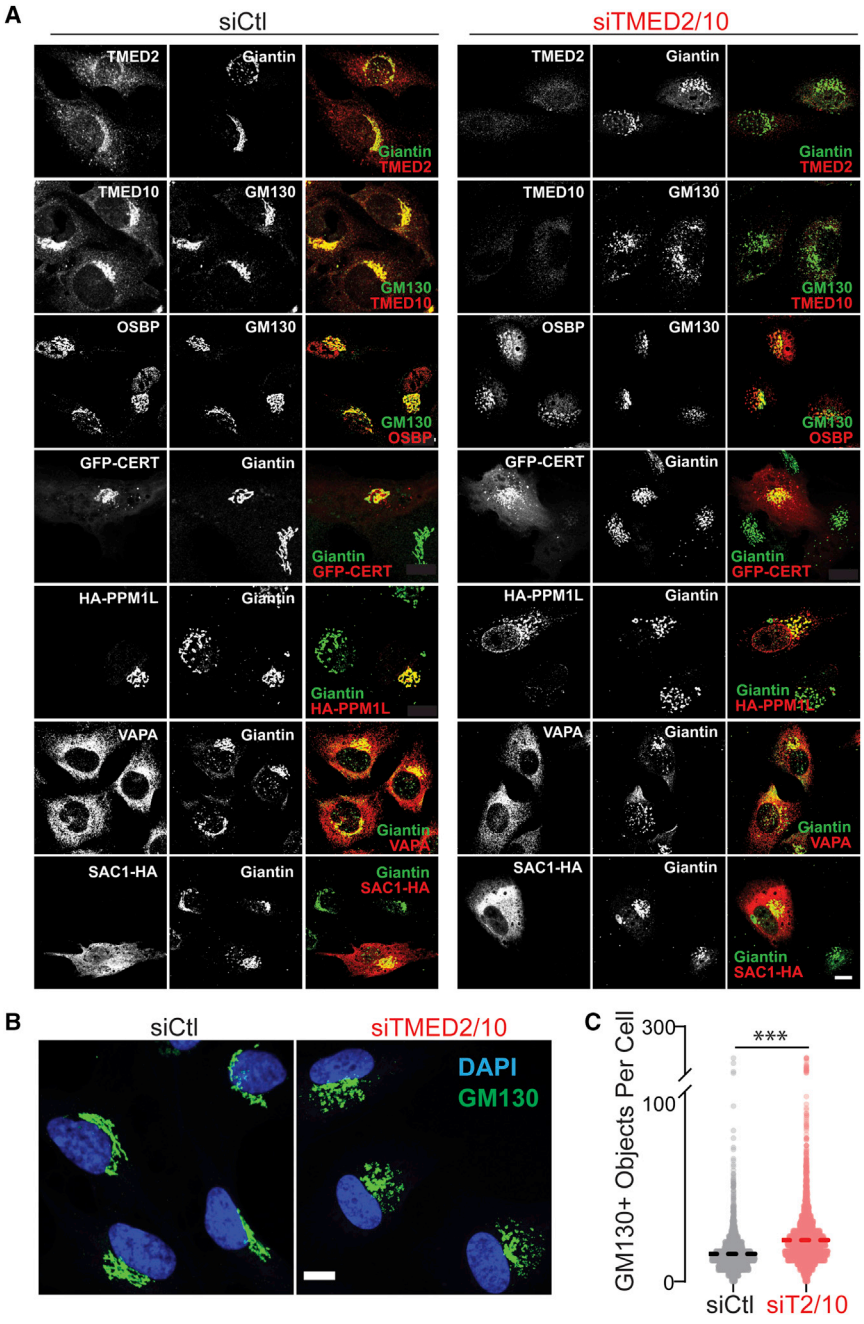

Figure 4. TMED2/10 affect Golgi morphology

(A) Control or silenced cells were stained for different MCS proteins and Golgi markers. Tagged versions of PPM1L, CERT, and SAC1 were over-expressed 24 h pre-fixation in all cells.

(B) Same as in (A).

(C) Cells in (B) were segmented by their labeled nuclei, and GM130-positive objects were quantified. n = 4,327, siCtl; n = 8,369, siTMED2/10 from three replicates. The average Golgi fragments per cell are shown. ***$p < 0.001$ (unpaired two-tailed t test). Results are mean ± SEM. All scale bars are 10 μm.

See also Figure S4.

TMED2/10 silencing does not affect the localization of ER-Golgi MCS components

Since TMED proteins have been shown to be cargo protein receptors, it is possible that they are required for proper localization of MCS components. We first looked at the localization of TMED2 and TMED10 in RPE1 cells, where co-localization with Golgi markers such as giantin (medial-Golgi), GM130 (*cis*-Golgi) (Figure 4A), and GOLPH3 (*trans*-Golgi) indicated an accumulation in the Golgi (Figure S4C). Similar localization was observed in HeLa cells (Figure S4C). Co-localization with Golgi markers was previously reported for the MCS proteins OSBP, CERT, and the CERT phosphatase PPM1L, which dephosphorylates CERT to enhance its membrane association (Mesmin et al., 2013, 2019; Saito et al., 2008), while it is well established that VAPA and SAC1 localize to the ER. These are all consistent with our observations (Figure 4A), and silencing TMED2/10 did not grossly affect the localization of these MCS components (Figure 4A). However, the staining did appear different due to an alteration of the Golgi morphology (Figures 4B and 4C), which was consistently fragmented.

Fragmentation of the Golgi has been previously reported upon upregulation of the SCD1 (Lita et al., 2021). Since SCD1 was upregulated in TMED2/10-silenced cells, we tested the effect of SCD1 inhibition (A939572) on the Golgi morphology in HeLa cells, which partially reverted the phenotype (Figures S4D and S4E). Since our previous data showed a recovery of plasma membrane cholesterol levels upon ACAT inhibition (Figures 3E and 3F), we asked whether this inhibition would also restore the Golgi morphology. Treatment of silenced cells with avasimibe indeed showed a significant reversion of Golgi fragmentation (Figures S4D and S4E).

Overall, our biochemical (Figures 2, 3, S2, and S3) and morphological analyses (Figures 4 and S4) suggest that TMED2/10 are directly involved in the transport of cholesterol at ER-Golgi MCSs.

TMED2/10 are required for the assembly of ER-Golgi MCS protein supercomplexes

Finally, we analyzed whether TMED2/10 are in fact integral members of the protein complexes at MCSs. We first determined whether TMED2/10 interact with known components of ER-Golgi MCSs by performing co-immunoprecipitation experiments. The immunoprecipitation (IP) of endogenous OSBP pulled down both TMED2 and TMED10 (Figures 5A and 5B).

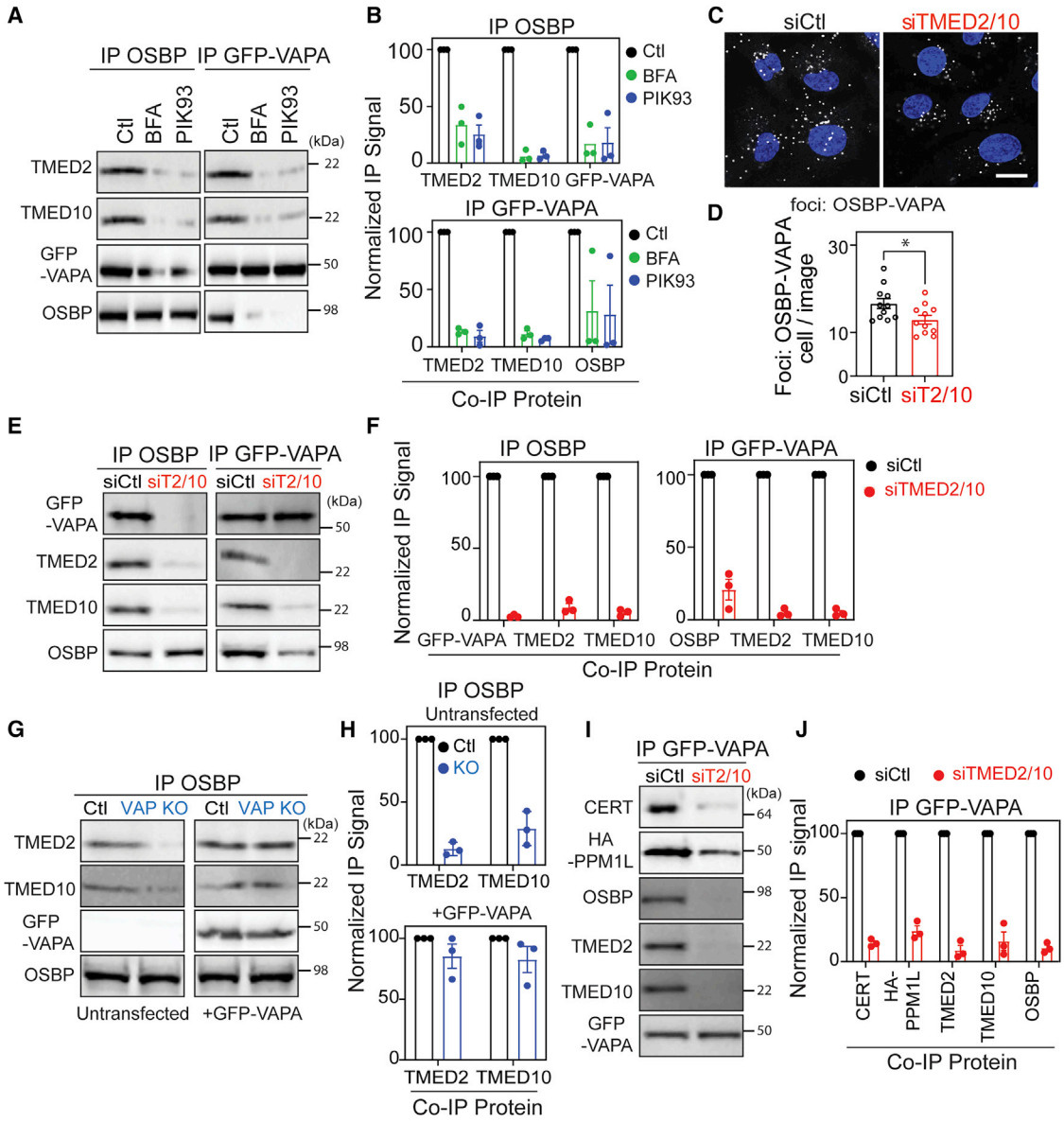

Figure 5. TMED2/10 interact with ER-Golgi MCS proteins and control PtdIns(4)P transfer

(A) Western blot of immunoprecipitated (IP) OSBP or IP GFP-VAPA fractions after BFA or PIK93 treatment. Cells were lysed post BFA (5 μg/mL for 5 min) or PIK93 (4 μM for 10 min) treatments, and subsequent IP was performed.

(B) The values for (A) were normalized, with the control set to 100.

(C) Antibody-based *in situ* proximity ligation assay was performed on pre-fixed and permeabilized siCtl and siTMED2/10 cells. Plus and minus probes were used to target rabbit anti-OSBP and mouse anti-VAPA antibodies.

(D) The number of foci were extracted per image in (C) and are shown normalized to the number of cells per image. n = 129, siCtl; n = 132, siTMED2/10. Scale bars, 10 μm. *$p < 0.05$ (unpaired two-tailed t test).

(E and F) Same as in (A) and (B), OSBP and GFP-VAPA IPs performed in control and siTMED2/10 cells. In (F), the coIP signal was set to 100 in siCtl cells.

(G and H) Same as in (E) and (F), GFP-VAPA IP was performed in cells overexpressing HA-PPM1L or GFP-CERT.

(I and J) Same as in (G) and (H), in HeLa control or VAP knockout cells either transfected with GFP-VAPA or not (untransfected). In (J), the coIP signal was set to 100 in control cells. Results are mean ± SEM ($n \geq 3$).

See also Figure S5.

Since the interaction of OSBP with the Golgi depends on the presence of ARF1 and PtdIns(4)P, we tested the effect of the fungal metabolite brefeldin-A (BFA), which inhibits ARF activation, and of the PI4P-kinase inhibitor PIK93 on the TMED2/10-OSBP interaction (Donaldson et al., 2005; Hsu et al., 2010). Our treatment times were chosen based on the release of OSBP from the Golgi. IP of OSBP after BFA (5 min) or PIK93 (10 min) treatment showed a loss of OSBP-TMED interaction (Figure S5A).

IP of GFP-VAPA also pulled down both TMED2 and TMED10 and showed that these interactions are impaired upon BFA

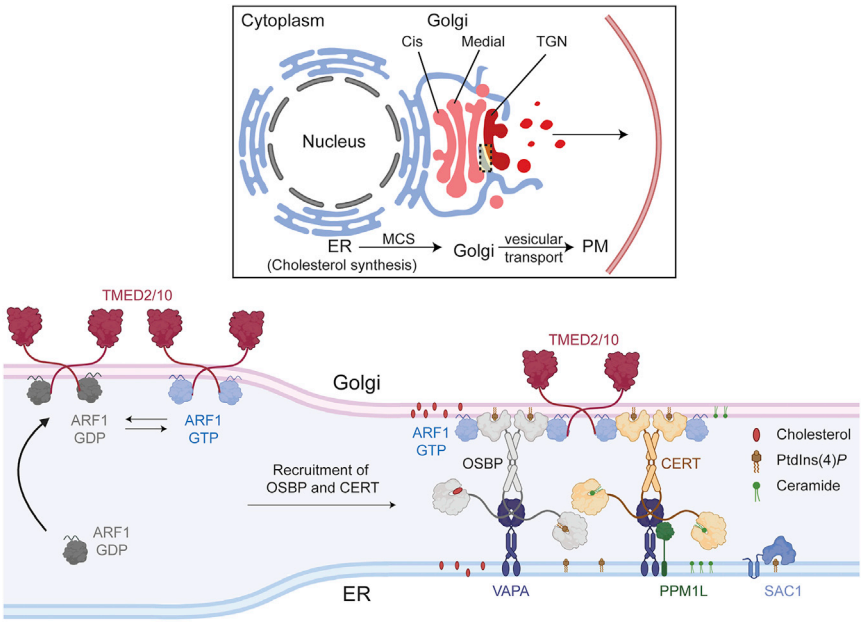

Figure 6. Molecular architecture of ER-Golgi membrane contact sites

Newly synthesized cholesterol is actively transferred from ER to the Golgi at ER-Golgi MCS. Once at the Golgi, the cholesterol reaches the plasma membrane via vesicular transport (top panel). At the ER-Golgi contacts (bottom panel), cytosolic ARF1-GDP binds Golgi membranes via its interaction with TMED cytosolic tail. Membrane-bound ARF1-GDP is then converted to GTP form by the action of a nucleotide exchange factor. ARF1-GTP subsequently recruits OSBP-VAPA and CERT-VAPA complexes to Golgi membranes. Altogether, Golgi-localized TMED2/10 and ARF1; ER-localized VAPA, PPM1L, and SAC1; and main transfer proteins OSBP and CERT form a mega-protein structure that constitutes the ER-Golgi MCS. Created with BioRender.com.

and PIK93 treatments (Figures 5C and 5D). These observations indicate that VAPA, OSBP, and TMED2/10 are part of a complex, which depends on the presence of PtdIns(4)P and ARF1.

We next tested whether TMED2/10 play a role in the formation or maintenance of ER-Golgi MCSs by monitoring the interaction of VAPA with OSBP using a proximity ligation assay and found it to be significantly decreased in TMED2/10-silenced cells (Figures 5C and 5D), despite the high level of background of this assay. IP of OSBP from TMED2/10-silenced cells completely failed to pull down GFP-VAPA, and vice versa, IP of GFP-VAPA failed to pull down OSBP (Figures 5E and 5F). We also tested whether the interaction between OSBP and TMED2/10 involves VAPA. IP of OSBP from VAPA/B knockout cells failed to pull down TMED2 and TMED10, and the interaction could be restored by recomplementing the cells with GFP-VAPA (Figures 5G and 5H).

Given our observations on the delayed production of sphingomyelin, we extended our biochemical analyses to include CERT and its phosphatase PPM1L. IP of GFP-VAPA pulled down both CERT and PPM1L in control cells, as expected, but this interaction was drastically reduced upon TMED2/10 silencing (Figures 5I and 5J). The interactions between VAPA, OSBP, and CERT could not be rescued by treating cells with the ACAT inhibitor avasimibe (Figures S5B and S5C), suggesting that it is the physical interactions between the proteins and not the Golgi integrity that maintain the complex in the presence of TMED2/10.

MCSs between the ER and the Golgi are well known to have two classes of complexes: one involved in cholesterol transfer, containing VAPA, SAC1, OSBP, and ARF1; and another involved in ceramide transfer, containing VAPA, PPM1L, and CERT. The above analysis shows not only that TMED2/10 are present in both these complexes and required for their existence but also that these two complexes actually can form supercomplexes, mediating the transfer of both cholesterol and ceramide, again in a TMED2/10-dependent manner (Figure 6).

DISCUSSION

To identify factors involved in the anthrax toxin entry process, we herein performed an RNAi screen. We identified two proteins, TMED2 and TMED10, and showed that they are involved in plasma membrane subcompartmentalization. While TMEDs are well established cargo receptors/chaperones of GPI-anchored proteins, we here determined that they are also key players of ER-Golgi MCSs, where they act as indispensable components of large protein supercomplexes responsible for intracellular lipid transport that controls the formation of cholesterol-rich plasma membrane nanodomains (Figure 6).

Elegant *in vitro* studies have shown that a VAPA-OSBP complex is sufficient to transfer cholesterol and PtdIns(4)P between vesicles (de la Mora et al., 2021). In living cells, this process in addition requires ARF1 that, by cycling between its GDP- and GTP-bound forms, contributes to the recruitment of OSBP at the ER-Golgi MCSs (Adarska et al., 2021; Donaldson et al., 2005; Nakatsu and Kawasaki, 2021). The mechanism that ensures initial recruitment of ARF1 at MCSs is not known. Interestingly, the cytosolic tail of TMED10 has been shown to directly interact with the GDP-bound form of ARF1 and to recruit it to the Golgi (Gommel, 2001; Zheng et al., 2013). Our work shows that the interaction between different components of the cholesterol transfer complex at ER-Golgi interfaces and their ability to transfer cholesterol are dependent on TMED2/10. It is then tempting to speculate that TMED2/10 prime the dynamic assembly of the lipid transferring machinery at ER-Golgi MCSs by guiding the local recruitment of ARF1 (Figure 6). Future studies will address whether and how the different functions reported of TMED proteins are connected, which include as cargo receptors ensuring the transport of the nanodomain-associated escorting GPI-anchored proteins (Castillon et al., 2011; Zavodszky and Hegde, 2019) or orchestrating MCSs (the present study).

Our work also shows that the cholesterol transfer and the ceramide transfer complexes are in fact part of a TMED2/10-dependent supercomplex, which offers interesting potential of co-regulation. The most stunning finding of our work is however that alterations in these supercomplexes can lead to a complete

loss of lipid nanodomains at the plasma membrane; thus, the transport of cholesterol via vesicular trafficking through the biosynthetic pathway is unable to compensate even with time. ER-Golgi MCSs therefore control plasma membrane compartmentalization, anthrax intoxication, and possibly other nanodomain-dependent cellular processes.

Limitations of the study

Our study identifies TMED2 and TMED10 as components of MCSs between the ER and the Golgi. Here, TMED2 and TMED10 are involved in lipid transfer by maintaining and bridging together two previously identified complexes operating non-vesicular transport of cholesterol and ceramide. Morphological and structural evidence for these MCS-located supercomplexes is currently limiting, possibly because of their transient nature. Moreover, we could not investigate how ER-Golgi MCSs are modified in the absence of TMED2 and TMED10 due to the fact that the structure of the Golgi and the ER are affected by the absence of these proteins. Further structural and morphological analyses would allow for a better understanding of these contacts and their dynamics and regulation. Future studies should also identify the full protein composition of these ER-Golgi MCSs.

STAR★METHODS

Detailed methods are provided in the online version of this paper and include the following:

SUPPLEMENTAL INFORMATION

Supplemental information can be found online at https://doi.org/10.1016/j.devcel.2022.09.004.

ACKNOWLEDGMENTS

We thank Pietro De Camilli Lab (Yale School of Medicine) for VAP KO cells; Hedge Lab (MRC Laboratory of Molecular Biology) for TMED10-HA plasmids; C. Gehin (EPFL) for HA-PPM1L construct; Holthuis Lab (University of Osnabrück) and G. Fairn (Dalhousie University) for D4-mCherry; Y. Hannun and D. Canals (Stony Brooks Cancer Centre) for lysenin-GFP; A. De Matteis (University of Napoli) for VAPA-GFP plasmid; F. Perez Lab (Institut Curie) for RUSH plasmid; D. Moreau and S. Vossio (ACCESS Geneva) for high-throughput imaging; J. Paz (EPFL) and T. Hannich (Molecular Discovery Platform, CeMM) for lipidomics; M. Leleu and F. David (BICC, EPFL) for RNA-seq analysis and data management; EPFL core facilities BIOP, GECF, FCCF, and BICC for sharing their equipment and expertise; all VDG and D'Angelo Lab members for the discussions; S. Ho for cloning and protein purification and manuscript editing; A. Samurkas for protein modeling; and N. Panyain for the schematics created with BioRender.com. This work was supported by the Swiss National Science Foundation grant to F.G.v.d.G. and to G.D'A.

AUTHOR CONTRIBUTIONS

M.U.A., O.A.S., L.A., G.D'A., and F.G.v.d.G. conceptualized the overall project, analyzed the results, and prepared the manuscript, with input from all co-authors. O.A.S. and I.L. performed the siRNA screen and its analysis, under the guidance of P.L., G.D'A., and F.G.v.d.G. For other experiments, M.U.A., O.A.S., L.A., F.S.M., T.A., A.C., and L.C. performed and analyzed the experiments, with guidance from G.D'A. and F.G.v.d.G.

DECLARATION OF INTERESTS

The authors declare no competing interests.

INCLUSION AND DIVERSITY

We support ethical, inclusive, diverse, and equitable conduct of research.

Received: May 13, 2022
Revised: July 24, 2022
Accepted: September 8, 2022
Published: September 28, 2022

REFERENCES

Abrami, L., Bischofberger, M., Kunz, B., Groux, R., and van der Goot, F.G. (2010a). Endocytosis of the anthrax toxin is mediated by clathrin, actin and unconventional adaptors. PLoS Pathog *6*, e1000792. https://doi.org/10.1371/journal.ppat.1000792.

Abrami, L., Kunz, B., and van der Goot, F.G. (2010b). Anthrax toxin triggers the activation of src-like kinases to mediate its own uptake. Proc. Natl. Acad. Sci. USA *107*, 1420–1424. https://doi.org/10.1073/pnas.0910782107.

Abrami, L., Leppla, S.H., and van der Goot, F.G. (2006). Receptor palmitoylation and ubiquitination regulate anthrax toxin endocytosis. J. Cell Biol. *172*, 309–320. https://doi.org/10.1083/jcb.200507067.

Abrami, L., Lindsay, M., Parton, R.G., Leppla, S.H., and van der Goot, F.G. (2004). Membrane insertion of anthrax protective antigen and cytoplasmic delivery of lethal factor occur at different stages of the endocytic pathway. J. Cell Biol. *166*, 645–651. https://doi.org/10.1083/jcb.200312072.

Abrami, L., Liu, S., Cosson, P., Leppla, S.H., and van der Goot, F.G. (2003). Anthrax toxin triggers endocytosis of its receptor via a lipid raft–mediated

clathrin-dependent process. J. Cell Biol. *160*, 321–328. https://doi.org/10.1083/jcb.200211018.

Adarska, P., Wong-Dilworth, L., and Bottanelli, F. (2021). ARF GTPases and their ubiquitous role in intracellular trafficking Beyond the Golgi. Front. Cell Dev. Biol. *9*, 679046. https://doi.org/10.3389/fcell.2021.679046.

Amen, T., and Kaganovich, D. (2021). Stress granules inhibit fatty acid oxidation by modulating mitochondrial permeability. Cell Rep *35*, 109237. https://doi.org/10.1016/j.celrep.2021.109237.

Antonny, B., Bigay, J., and Mesmin, B. (2018). The oxysterol-binding protein cycle: burning off PI(4)P to transport cholesterol. Annu. Rev. Biochem. *87*, 809–837. https://doi.org/10.1146/annurev-biochem-061516-044924.

Bausch-Fluck, D., Hofmann, A., Bock, T., Frei, A.P., Cerciello, F., Jacobs, A., Moest, H., Omasits, U., Gundry, R.L., Yoon, C., et al. (2015). A mass spectrometric-derived cell surface protein atlas. PLoS One *10*, e0121314. https://doi.org/10.1371/journal.pone.0121314.

Bindea, G., Galon, J., and Mlecnik, B. (2013). CluePedia cytoscape plugin: pathway insights using integrated experimental and in silico data. Bioinformatics *29*, 661–663. https://doi.org/10.1093/bioinformatics/btt019.

Bindels, D.S., Haarbosch, L., van Weeren, L., Postma, M., Wiese, K.E., Mastop, M., Aumonier, S., Gotthard, G., Royant, A., Hink, M.A., and Gadella, T.W.J. (2017). mScarlet: A bright monomeric red fluorescent protein for cellular imaging. Nat. Methods *14*, 53–56. https://doi.org/10.1038/nmeth.4074.

Boncompain, G., Divoux, S., Gareil, N., de Forges, H., Lescure, A., Latreche, L., Mercanti, V., Jollivet, F., Raposo, G., and Perez, F. (2012). Synchronization of secretory protein traffic in populations of cells. Nat. Methods *9*, 493–498. https://doi.org/10.1038/nmeth.1928.

Bürgi, J., Abrami, L., Castanon, I., Abriata, L.A., Kunz, B., Yan, S.E., Lera, M., Unger, S., Superti-Furga, A., Peraro, M.D., et al. (2020). Ligand binding to the collagen VI receptor triggers a talin-to-RhoA switch that regulates receptor endocytosis. Dev. Cell *53*, 418–430.e4. https://doi.org/10.1016/j.devcel.2020.04.015.

Canals, D., Salamone, S., and Hannun, Y.A. (2018). Visualizing bioactive ceramides. Chem. Phys. Lipids *216*, 142–151. https://doi.org/10.1016/j.chemphyslip.2018.09.013.

Capasso, S., Sticco, L., Rizzo, R., Pirozzi, M., Russo, D., Dathan, N.A., Campelo, F., van Galen, J., Hölttä-Vuori, M., Turacchio, G., et al. (2017). Sphingolipid metabolic flow controls phosphoinositide turnover at the *trans* -Golgi network. EMBO J *36*, 1736–1754. https://doi.org/10.15252/embj.201696048.

Castillon, G.A., Aguilera-Romero, A., Manzano-Lopez, J., Epstein, S., Kajiwara, K., Funato, K., Watanabe, R., Riezman, H., and Muñiz, M. (2011). The yeast p24 complex regulates GPI-anchored protein transport and quality control by monitoring anchor remodeling. Mol. Biol. Cell *22*, 2924–2936. https://doi.org/10.1091/mbc.E11-04-0294.

Contreras, F.-X., Ernst, A.M., Haberkant, P., Björkholm, P., Lindahl, E., Gönen, B., Tischer, C., Elofsson, A., von Heijne, G., Thiele, C., et al. (2012). Molecular recognition of a single sphingolipid species by a protein's transmembrane domain. Nature *481*, 525–529. https://doi.org/10.1038/nature10742.

de la Mora, E., Dezi, M., Di Cicco, A., Bigay, J., Gautier, R., Manzi, J., Polidori, J., Castaño-Díez, D., Mesmin, B., Antonny, B., and Lévy, D. (2021). Nanoscale architecture of a VAP-A-OSBP tethering complex at membrane contact sites. Nat. Commun. *12*, 3459. https://doi.org/10.1038/s41467-021-23799-1.

Donaldson, J.G., Honda, A., and Weigert, R. (2005). Multiple activities for Arf1 at the Golgi complex. Biochim. Biophys. Acta *1744*, 364–373. https://doi.org/10.1016/j.bbamcr.2005.03.001.

Dong, R., Saheki, Y., Swarup, S., Lucast, L., Harper, J.W., and De Camilli, P. (2016). Endosome-ER contacts control actin nucleation and retromer function through VAP-dependent regulation of PI4P. Cell *166*, 408–423. https://doi.org/10.1016/j.cell.2016.06.037.

Dorfer, V., Pichler, P., Stranzl, T., Stadlmann, J., Taus, T., Winkler, S., and Mechtler, K. (2014). MS Amanda, a universal identification algorithm optimized for high accuracy tandem mass spectra. J. Proteome Res. *13*, 3679–3684. https://doi.org/10.1021/pr500202e.

Edgar, R., Domrachev, M., and Lash, A.E. (2002). Gene Expression Omnibus: NCBI gene expression and hybridization array data repository. Nucleic Acids Res *30*, 207–210. https://doi.org/10.1093/nar/30.1.207.

Emery, G., Rojo, M., and Gruenberg, J. (2000). Coupled transport of p24 family members. J. Cell Sci. *113*, 2507–2516. https://doi.org/10.1242/jcs.113.13.2507.

Friebe, S., van der Goot, F.G., and Bürgi, J. (2016). The ins and outs of anthrax toxin. Toxins *8*, 69. https://doi.org/10.3390/toxins8030069.

Gommel, D., Orci, L., Emig, E.M., Hannah, M.J., Ravazzola, M., Nickel, W., Helms, J.B., Wieland, F.T., and Sohn, K. (1999). p24 and p23, the major transmembrane proteins of COPI-coated transport vesicles, form hetero-oligomeric complexes and cycle between the organelles of the early secretory pathway. FEBS Lett *447*, 179–185. https://doi.org/10.1016/S0014-5793(99)00246-X.

Gommel, D.U., Memon, A.R., Heiss, A., Lottspeich, F., Pfannstiel, J., Lechner, J., Reinhard, C., Helms, J.B., Nickel, W., and Wieland, F.T. (2001). Recruitment to Golgi membranes of ADP-ribosylation factor 1 is mediated by the cytoplasmic domain of p23. EMBO J *20*, 6751–6760. https://doi.org/10.1093/emboj/20.23.6751.

Hanada, K., Kumagai, K., Tomishige, N., and Yamaji, T. (2009). CERT-mediated trafficking of ceramide. Biochim. Biophys. Acta *1791*, 684–691. https://doi.org/10.1016/j.bbalip.2009.01.006.

Hanada, K., Kumagai, K., Yasuda, S., Miura, Y., Kawano, M., Fukasawa, M., and Nishijima, M. (2003). Molecular machinery for non-vesicular trafficking of ceramide. Nature *426*, 803–809. https://doi.org/10.1038/nature02188.

Hsu, N.-Y., Ilnytska, O., Belov, G., Santiana, M., Chen, Y.-H., Takvorian, P.M., Pau, C., van der Schaar, H., Kaushik-Basu, N., Balla, T., et al. (2010). Viral reorganization of the secretory pathway generates distinct organelles for RNA replication. Cell *141*, 799–811. https://doi.org/10.1016/j.cell.2010.03.050.

Ikonen, E., and Zhou, X. (2021). Cholesterol transport between cellular membranes: A balancing act between interconnected lipid fluxes. Dev. Cell *56*, 1430–1436. https://doi.org/10.1016/j.devcel.2021.04.025.

Jiménez-Rojo, N., Leonetti, M.D., Zoni, V., Colom, A., Feng, S., Iyengar, N.R., Matile, S., Roux, A., Vanni, S., Weissman, J.S., and Riezman, H. (2020). Conserved functions of ether lipids and sphingolipids in the early secretory pathway. Curr. Biol. *30*, 3775–3787.e7. https://doi.org/10.1016/j.cub.2020.07.059.

Kamentsky, L., Jones, T.R., Fraser, A., Bray, M.-A., Logan, D.J., Madden, K.L., Ljosa, V., Rueden, C., Eliceiri, K.W., and Carpenter, A.E. (2011). Improved structure, function and compatibility for CellProfiler: modular high-throughput image analysis software. Bioinformatics *27*, 1179–1180. https://doi.org/10.1093/bioinformatics/btr095.

Klimpel, K.R., Molloy, S.S., Thomas, G., and Leppla, S.H. (1992). Anthrax toxin protective antigen is activated by a cell surface protease with the sequence specificity and catalytic properties of furin. Proc. Natl. Acad. Sci. USA *89*, 10277–10281. https://doi.org/10.1073/pnas.89.21.10277.

Kong, A.T., Leprevost, F.V., Avtonomov, D.M., Mellacheruvu, D., and Nesvizhskii, A.I. (2017). MSFragger: ultrafast and comprehensive peptide identification in mass spectrometry–based proteomics. Nat. Methods *14*, 513–520. https://doi.org/10.1038/nmeth.4256.

Krantz, B.A., Finkelstein, A., and Collier, R.J. (2006). Protein translocation through the anthrax toxin transmembrane pore is driven by a proton gradient. J. Mol. Biol. *355*, 968–979. https://doi.org/10.1016/j.jmb.2005.11.030.

Larios, J., Mercier, V., Roux, A., and Gruenberg, J. (2020). ALIX- and ESCRT-III–dependent sorting of tetraspanins to exosomes. J. Cell Biol. *219*, e201904113. https://doi.org/10.1083/jcb.201904113.

Levental, I., Levental, K.R., and Heberle, F.A. (2020). Lipid rafts: controversies resolved, mysteries remain. Trends Cell Biol *30*, 341–353. https://doi.org/10.1016/j.tcb.2020.01.009.

Levine, T.P., and Munro, S. (2002). Targeting of Golgi-specific pleckstrin homology domains involves both PtdIns 4-kinase-dependent and -independent components. Curr. Biol. *12*, 695–704. https://doi.org/10.1016/S0960-9822(02)00779-0.

Liberali, P., Snijder, B., and Pelkmans, L. (2014). A hierarchical map of regulatory genetic interactions in membrane trafficking. Cell *157*, 1473–1487. https://doi.org/10.1016/j.cell.2014.04.029.

Lita, A., Pliss, A., Kuzmin, A., Yamasaki, T., Zhang, L., Dowdy, T., Burks, C., de Val, N., Celiku, O., Ruiz-Rodado, V., et al. (2021). IDH1 mutations induce organelle defects via dysregulated phospholipids. Nat. Commun. *12*, 614. https://doi.org/10.1038/s41467-020-20752-6.

Luo, J., Yang, H., and Song, B.-L. (2020). Mechanisms and regulation of cholesterol homeostasis. Nat. Rev. Mol. Cell Biol. *21*, 225–245. https://doi.org/10.1038/s41580-019-0190-7.

Maekawa, M., and Fairn, G.D. (2015). Complementary probes reveal that phosphatidylserine is required for the proper transbilayer distribution of cholesterol. J. Cell Sci. *128*, 1422–1433. https://doi.org/10.1242/jcs.164715.

Mañes, S., del Real, G., and Martínez-A, C. (2003). Pathogens: raft hijackers. Nat. Rev. Immunol. *3*, 557–568. https://doi.org/10.1038/nri1129.

Maxfield, F.R., and Wüstner, D. (2012). Analysis of cholesterol trafficking with fluorescent probes. Methods Cell Biol *108*, 367–393. https://doi.org/10.1016/B978-0-12-386487-1.00017-1.

McCaffrey, M.W., Bielli, A., Cantalupo, G., Mora, S., Roberti, V., Santillo, M., Drummond, F., and Bucci, C. (2001). Rab4 affects both recycling and degradative endosomal trafficking. FEBS Lett *495*, 21–30. https://doi.org/10.1016/S0014-5793(01)02359-6.

Mesmin, B., Bigay, J., Moser von Filseck, J., Lacas-Gervais, S., Drin, G., and Antonny, B. (2013). A four-step cycle driven by PI(4)P hydrolysis directs sterol/PI(4)P exchange by the ER-Golgi tether OSBP. Cell *155*, 830–843. https://doi.org/10.1016/j.cell.2013.09.056.

Mesmin, B., Kovacs, D., and D'Angelo, G. (2019). Lipid exchange and signaling at ER–Golgi contact sites. Curr. Opin. Cell Biol. *57*, 8–15. https://doi.org/10.1016/j.ceb.2018.10.002.

Mesquita, F.S., van der Goot, F.G., and Sergeeva, O.A. (2020). Mammalian membrane trafficking as seen through the lens of bacterial toxins. Cell. Microbiol. *22*, e13167. https://doi.org/10.1111/cmi.13167.

Milne, J.C., Furlong, D., Hanna, P.C., Wall, J.S., and Collier, R.J. (1994). Anthrax protective antigen forms oligomers during intoxication of mammalian cells. J. Biol. Chem. *269*, 20607–20612. https://doi.org/10.1016/S0021-9258(17)32036-7.

Moreau, D., Vacca, F., Vossio, S., Scott, C., Colaco, A., Paz Montoya, J., Ferguson, C., Damme, M., Moniatte, M., Parton, R.G., et al. (2019). Drug-induced increase in lysobisphosphatidic acid reduces the cholesterol overload in Niemann–Pick type C cells and mice. EMBO Rep *20*, e47055. https://doi.org/10.15252/embr.201847055.

Munro, S. (2003). Lipid rafts: elusive or illusive? Cell *115*, 377–388. https://doi.org/10.1016/S0092-8674(03)00882-1.

Nakatsu, F., and Kawasaki, A. (2021). Functions of oxysterol-binding proteins at membrane contact sites and their control by phosphoinositide metabolism. Front. Cell Dev. Biol. *9*, 664788. https://doi.org/10.3389/fcell.2021.664788.

Park, J.M., Greten, F.R., Li, Z.-W., and Karin, M. (2002). Macrophage apoptosis by anthrax lethal factor Through p38 MAP kinase inhibition. Science *297*, 2048–2051. https://doi.org/10.1126/science.1073163.

Pelkmans, L., and Zerial, M. (2005). Kinase-regulated quantal assemblies and kiss-and-run recycling of caveolae. Nature *436*, 128–133. https://doi.org/10.1038/nature03866.

Perez-Riverol, Y., Bai, J., Bandla, C., García-Seisdedos, D., Hewapathirana, S., Kamatchinathan, S., Kundu, D.J., Prakash, A., Frericks-Zipper, A., Eisenacher, M., et al. (2022). The PRIDE database resources in 2022: a hub for mass spectrometry-based proteomics evidences. Nucleic Acids Res *50*, D543–D552. https://doi.org/10.1093/nar/gkab1038.

R Core Team. (2019). R: A Language and Environment for Statistical Computing (R Foundation for Statistical Computing). https://www.R-project.org/.

Ramachandran, R., Heuck, A.P., Tweten, R.K., and Johnson, A.E. (2002). Structural insights into the membrane-anchoring mechanism of a cholesterol-dependent cytolysin. Nat. Struct. Biol. *9*, 823–827. https://doi.org/10.1038/nsb855.

Rappsilber, J., Mann, M., and Ishihama, Y. (2007). Protocol for micro-purification, enrichment, pre-fractionation and storage of peptides for proteomics using StageTips. Nat. Protoc. *2*, 1896–1906. https://doi.org/10.1038/nprot.2007.261.

Robinson, M.D., McCarthy, D.J., and Smyth, G.K. (2010). edgeR: A Bioconductor package for differential expression analysis of digital gene expression data. Bioinformatics *26*, 139–140. https://doi.org/10.1093/bioinformatics/btp616.

Saito, S., Matsui, H., Kawano, M., Kumagai, K., Tomishige, N., Hanada, K., Echigo, S., Tamura, S., and Kobayashi, T. (2008). Protein phosphatase 2Cε is an endoplasmic reticulum integral membrane protein that dephosphorylates the ceramide transport protein CERT to enhance its association with organelle membranes. J. Biol. Chem. *283*, 6584–6593. https://doi.org/10.1074/jbc.M707691200.

Schiavo, G., and van der Goot, F.G. (2001). The bacterial toxin toolkit. Nat. Rev. Mol. Cell Biol. *2*, 530–537. https://doi.org/10.1038/35080089.

Schindelin, J., Arganda-Carreras, I., Frise, E., Kaynig, V., Longair, M., Pietzsch, T., Preibisch, S., Rueden, C., Saalfeld, S., Schmid, B., et al. (2012). Fiji: an open-source platform for biological-image analysis. Nat. Methods *9*, 676–682. https://doi.org/10.1038/nmeth.2019.

Sergeeva, O.A., and van der Goot, F.G. (2019). Anthrax toxin requires ZDHHC5-mediated palmitoylation of its surface-processing host enzymes. Proc. Natl. Acad. Sci. USA *116*, 1279–1288. https://doi.org/10.1073/pnas.1812588116.

Strating, J.R.P.M., and Martens, G.J.M. (2009). The p24 family and selective transport processes at the ER-Golgi interface. Biol. Cell *101*, 495–509. https://doi.org/10.1042/BC20080233.

Sun, J., and Jacquez, P. (2016). Roles of anthrax toxin Receptor 2 in anthrax toxin membrane insertion and pore formation. Toxins *8*, 34. https://doi.org/10.3390/toxins8020034.

Takahashi, M., Murate, M., Fukuda, M., Sato, S.B., Ohta, A., and Kobayashi, T. (2007). Cholesterol controls lipid endocytosis through Rab11 Rab11□D. Mol. Biol. Cell *18*, 2667–2677.

Venditti, R., Rega, L.R., Masone, M.C., Santoro, M., Polishchuk, E., Sarnataro, D., Paladino, S., D'Auria, S., Varriale, A., Olkkonen, V.M., et al. (2019). Molecular determinants of ER–Golgi contacts identified through a new FRET–FLIM system. J Cell Biol. *218*, 1055–1065. https://doi.org/10.1083/jcb.201812020.

Whitfield, G.B., Brock, T.D., Ammann, A., Gottlieb, D., and Carter, H.E. (1955). Filipin, an antifungal antibiotic: isolation and properties. J. Am. Chem. Soc. *77*, 4799–4801. https://doi.org/10.1021/ja01623a032.

Zavodszky, E., and Hegde, R.S. (2019). Misfolded GPI-anchored proteins are escorted through the secretory pathway by ER-derived factors. eLife *8*, e46740. https://doi.org/10.7554/eLife.46740.

Zheng, P., Gao, F., Deng, K., Gong, W., and Sun, Z. (2013). Expression, purification and preliminary X-ray crystallographic analysis of Arf1-GDP in complex with dimeric p23 peptide. Acta Crystallogr. Sect. F Struct. Biol. Cryst. Commun. *69*, 1155–1158. https://doi.org/10.1107/S1744309113024330.

STAR★METHODS

KEY RESOURCES TABLE

Reagent or resource	Source	Identifier
Antibodies		
Rabbit anti-MEK2	Santa Cruz Biotechnology	Cat# sc-523; RRID: AB_2281672
Mouse anti-EEA1	BD Biosciences	Cat# 610457; RRID: AB_397830
Goat anti-PA (*B. Anthracis*)	List Biological Laboratories	Cat# 771B
Mouse anti-GAPDH	Sigma-Aldrich	Cat# G8795; RRID: AB_1078991
Rabbit anti-CMG2	Proteintech Group	Cat# 16723-1-AP; RRID: AB_2056741
Rabbit anti-OSBP	Atlas antibodies	Cat# HPA039227; RRID: AB_2676401
Rabbit anti-CERT	Novus Biologicals	Cat# NB 100-2114; RRID: AB_535603
Rabbit anti-CLIMP63	Bethyl Laboratories	Cat# A302-257A; RRID: AB_1731083
Rabbit anti-caveolin1	Santa Cruz Biotechnology	Cat# sc-894; RRID: AB_2072042
Rat anti-HA-HRP	Roche Diagnostics	Cat# 12013819001; RRID: AB_390917
Mouse anti-V5	Thermo Fisher Scientific	Cat# R960-25; RRID: AB_2556564
Mouse anti-VAPA	Santa Cruz Biotechnology	Cat# sc-293278; RRID: AB_2801294
Mouse anti-TMED2	Santa Cruz Biotechnology	Cat# sc-376459; RRID: AB_11150297
Rabbit anti-TMED10	Bethyl Laboratories	Cat# A305-219A; RRID: AB_2631612
Rabbit anti-GOLPH3	Abcam	Cat# ab98023; RRID: AB_10860828
Mouse anti-GM130	BD Biosciences	Cat# 610823; RRID: AB_398142
Rabbit anti-Giantin	Biolegend	Cat#94302; RRID: AB_2801254
Mouse anti-GFP	Roche Diagnostics	Cat# 11814460001; RRID: AB_390913
Rabbit anti-CERT	Abcam	Cat# ab151285; RRID: AB_2923087
Mouse anti-PtdIns(4)P	Echelon Biosciences	Cat# Z-P004; RRID: AB_11127796
Anti-mouse-Alexa488	ThermoFisher Scientific	Cat# A-11029; RRID: AB_2534088
Anti-mouse-Alexa568	ThermoFisher Scientific	Cat# A-10037; RRID: AB_2534013
Anti-mouse-Alexa647	ThermoFisher Scientific	Cat# A-31571; RRID: AB_162542
Anti-rabbit-Alexa488	ThermoFisher Scientific	Cat# A-21206; RRID: AB_2535792
Anti-rabbit-Alexa568	ThermoFisher Scientific	Cat# A-10042; RRID: AB_2534017
Anti-rabbit-Alexa647	ThermoFisher Scientific	Cat# A-31573; RRID: AB_2536183
Anti-mouse-HRP	GE Healthcare	Cat# NA931V; RRID: AB_772210
Anti-rabbit-HRP	GE Healthcare	Cat# NA934V; RRID: AB_772206
Anti-rat-HRP	GE Healthcare	Cat# NA935V; RRID: AB_2923088
Anti-goat-HRP	Sigma-Aldrich	Cat# A5420; RRID: AB_258242
Chemicals, peptides, and recombinant proteins		
Lysenin-GFP	Y. Hannun & D. Canals (Stony Brooks Cancer Centre)	Canals et al., 2018
D4-mCherry	J. Holthius & G. Fairn (University of Osnabruck & Dalhousie University)	Maekawa and Fairn, 2015
Protective antigen (PA^{83})	This study	Abrami et al., 2003
Protective antigen (PA^{63})	This study	Abrami et al., 2003
Lethal Factor (LF)	This study	Abrami et al., 2003
DMEM-GlutaMax	Gibco	Cat# 31966
MEM	Sigma-Aldrich	Cat# M4655
Glasgow Minimal Essential Media	Sigma-Aldrich	Cat# G6148
Fetal Bovine Serum	Pan Biotech	Cat# P30-3033
L-glutamine	Gibco	Cat# 25030081

(*Continued on next page*)

Continued

Reagent or resource	Source	Identifier
NEAA Solution	Gibco	Cat# 11140035
Trypan Blue	Sigma-Aldrich	Cat# T5526
Filipin III	Sigma-Aldrich	Cat# F4767
Nile Red	Sigma-Aldrich	Cat# 72485
Avasimibe	Sigma-Aldrich	Cat# PZ0190
Mirus TransIT-X2	Mirus Bio Corporation	Cat# MIR6000
RotiFect	Carl Roth	Cat# P001.1
Lipofectamine RNAiMAX	Thermo Fisher	Cat# 13778075
PBS	BioConcept	Cat# 3-05F29-I
Paraformaldehyde	Electron Microscopy Sciences	Cat# 15714
OptiMEM	Thermo Fisher	Cat# 31985062
SYBR Green Master Mix	Roche	Cat# 4913914001
Bovine Serum Albumin	Roche	Cat# K41-001
OptiPrep	Axis Shield	Cat# 1114542
Protease Inhibitor Cocktail	Sigma-Aldrich	Cat# 11836153001
Prolong Glass Antifade Mountant	Thermo Fisher	Cat# P36980
Protein G-coupled Sepharose beads	Sigma-Aldrich	Cat# 17-0618-01
Biotinylation solution (EZ-link)	Thermo Fisher	Cat# 21327
Bicinchoninic acid (BCA) protein assay solution	Interchim Uptima	Cat# 40840A
Critical commercial assays		
DuoLink PLA	Sigma-Aldrich	Cat# DUO92002, DUO92004
FITC BrdU Flow Kit	BD Biosciences	Cat# 559619
Alkaline-phosphatase activity kit (Colorimetric)	Abcam	Cat# ab83369
RNAeasy	Qiagen	Cat# 74004
iScript III	Bio-Rad	Cat# 1708891
QuikChange II XL	Agilent	Cat# 200522
Deposited data		
Proteomics	This study	PRIDE: PXD036511
RNA-seq	This study	GEO: GSE212660
Lipidomics	This study	Lipidomes: lxE2361
Unprocessed Western blots	This study	Mendeley Data: https://doi.org/10.17632/z8w3bwg2z7.1
Experimental model: Cell lines		
RPE1	ATCC	RRID: CVCL_4388
HeLa	ATCC	RRID: CVCL_0030
HeLa-MZ	N/A	Pelkmans and Zerial, 2005
HeLa-M WT	P. De Camilli (Yale School of Medicine)	Dong et al., 2016
HeLa-M VAP-KO	P. De Camilli (Yale School of Medicine)	Dong et al., 2016
Oligonucleotides		
Silencing (si)RNA	Table S3	
Primers (QPCR/QuikChange)	Table S4	
Recombinant DNA		
peGFP-VAPA	A. De Matteis (University of Napoli, Frederico II)	N/A
pcDNA3_TMED10-HA	R. Hedge (MRC, UK)	Zavodszky and Hegde, 2019
pcDNA3_TMED10-ΔGOLD	R. Hedge (MRC, UK)	Zavodszky and Hegde, 2019
pcDNA3_TMED10-ΔCC	R. Hedge (MRC, UK)	Zavodszky and Hegde, 2019
Str-KDEL_SBP-EGFP-GPI	F. Perez (Intitut Curie)	Boncompain et al., 2012
pmScarlet-i_Giantin-C1	Addgene (#58050)	Bindels et al., 2017

(*Continued on next page*)

Continued

Reagent or resource	Source	Identifier
pcDNA3.1_CALR21-mCherry-KDEL	This study	Amen and Kaganovich, 2021
pcDNA3_TMED10 R209S;R210S-HA	This study	N/A
pcDNA3_TMED10 K213E-HA	This study	N/A
pcDNA3_TMED10 R209S;R210S;K213E-HA	This study	N/A
pcDNA6.3_TMED2-V5	This study	N/A
peGFP-CERT	This study	N/A
pcDNA6.2_HA-PPM1L	This study	N/A
pcDNA3_SAC1-HA	This study	N/A
Software and algorithms		
Fiji ImageJ	Fiji	Schindelin et al., 2012
LAS-X	Leica	N/A
GraphPad Prism 9	GraphPad Software, Inc.	N/A
Cytoscape v3.7	Cytoscape Team	Bindea et al., 2013
edgeR v(3.30.3)	R Core Team	Robinson et al., 2010
FlowJo v10	BD Biosciences	N/A

RESOURCE AVAILABILITY

Lead contact

Please contact F. Gisou van der Goot (gisou.vandergoot@epfl.ch) for further information and to request materials used in this study.

Materials availability

TMED10 cytosolic tail mutants, TMED2-V5, GFP-CERT, HA-PPM1L, SAC1-HA and pSEAP2_secALP were generated for this study. Lethal Factor (LF) and protective antigen (PA) were home purified. These materials can be requested by contacting the lead contact.

Data and code availability

- The RNA-seq data discussed in this publication have been deposited in NCBI's Gene Expression Omnibus (Edgar et al., 2002) and are accessible through GEO Series accession number. Lipidomics data can be accessed at Lipidomes (EPFL) and the mass Spectrometry proteomics data are submitted to ProteomeXchange via the PRIDE partner repository (Perez-Riverol et al., 2022). Original western blot images have been deposited at Mendeley Data. key resources table Accession numbers/ DOI of these publicly available datasets are listed in the key resources table. Microscopy data reported in this paper will be shared by the lead contact upon request.
- This paper does not report any original code.
- Any additional information required to reanalyze the data reported in this paper is available from the lead contact upon request.

EXPERIMENTAL MODEL AND SUBJECT DETAILS

Cell lines and tissue culture

RPE1, HeLa, and HeLa-MZ, HeLa-M and HeLa-M VAP KO cells were used in this study. RPE1 were grown in DMEM GlutaMAX supplemented with 10% FBS and 2 mM antibiotics (P/S: penicillin and streptomycin). HeLa, HeLa-MZ, HeLa-M and HeLa-M VAP KO cells were grown in MEM supplemented with 10% FBS, 2 mM L-glutamine, and 1X MEM Non-Essential Amino Acid Solution and 2 mM antibiotics (P/S). Cells were grown under controlled conditions (37 °C; 95% air, 5% CO_2). Experiments were conducted using RPE1 cells, except indicated otherwise.

Cell lines were authenticated by Microsynth (Balgach, Switzerland). For HeLa and HeLa-MZ cell lines, the analyses showed 100% identity to the DNA profile of the cell line HeLa (ATCC: CCL2, RRID: CVCL_0030). RPE1 cells matched 100% to the DNA profile of the cell line hTERT RPE-1 (ATCC: CRL-4000, RRID: CVCL_4388). HeLa-M control and VAP KO cells were a kind gift from Prof. Pietro De Camilli (Yale, USA). The VAP knockouts were confirmed by PCR genotyping and sequencing (Dong et al., 2016).

METHOD DETAILS

Gene silencing and overexpression

Genes were silenced using siRNAs obtained from Qiagen (see Table S3 for sequences). Silencing was performed for 72–96 h using Lipofectamine RNAiMAX or INTERFERrin following the manufacturer's protocol. Silencing efficiency was checked via Western blot

and/or qPCR. TMED10-HA constructs were a kind gift from Prof. Ramanujan Hedge, MRC laboratory, UK. All point mutations were generated using QuikChange XL kit. Plasmids were expressed in RPE1 or HeLa cells for 24–48 h using TransIT-LT1 or ROTI-Fect transfection reagents or Neon Electroporation following the manufacturer's protocol.

Screening

The siRNA screen consisted of the four 384-well plates used in the Endocytome screens (Liberali et al., 2014) and one extra 384-well plate with genes that code for surface proteins. The extra plate was designed using cell surface mass spectrometry data in RPE1, the cell surface protein atlas (Bausch-Fluck et al., 2015) and known surface GPI-anchored proteins. Plates were ordered with pools of three Ambion Silencer Select siRNAs per gene (Thermo Fisher Scientific). The screen used reverse transfection of siRNAs in which all wells had 250 nM siRNA concentration in 10 μL of Opti-MEM (Gibco; Thermo Fisher Scientific). Lipofectamine2000 (Thermo Fisher Scientific) transfection reagent was added in at 0.05 μL in 5 μL of Opti-MEM per well. Cells were plated into a transfection mix at 800 per well in 50 μL of complete media. After 72 h of growth, cells were treated with anthrax toxin (0.5 μg/mL PA and 0.1 μg/mL LF) in minimal media (Glasgow minimal essential media (Sigma-Aldrich G6148) buffered with 10 mM HEPES) and incubated at 4 °C for 1 h. Wells were washed twice with complete media and plates were shifted to 37 °C for 1.5 h. After which, wells were fixed with 4% PFA in PBS for 15 min, quenched with 50 mM NH_4Cl in PBS for 10 min, permeabilized with 0.1% TritonX in PBS for 5 min, with 2 PBS washes between all steps. Next, cells were blocked with 0.5% BSA in PBS for 30 min and primary antibodies (rabbit anti-MEK2N 1:100 and mouse anti-EEA1 1:200) were applied in blocking buffer for 1 h, after which secondary antibodies (Alexa488 anti-rabbit and Alexa-568 anti-mouse both at 1:600) were applied in blocking buffer for 45 min. Finally, DAPI was applied at 0.4 μg/mL final in PBS for 10 min and CellTrace (Alexa 647 at 1:5000) in carbonate buffer was applied for 5 min. Wells were washed with PBS twice between steps and kept in PBS for imaging. Imaging was done using the Yokogawa CV7000S using the 20X objective and imaging the full well. Z-stack sums for each image were stitched together for the full well image.

Screen segmentation and quantification

The wells/siRNAs of the screens were quantified using CellProfiler (Kamentsky et al., 2011). Briefly, the images were separated into the four channels: DAPI, MEK2N, CellTrace, and EEA1. For the toxin entry, looking at MEK2 cleavage and therefore, disappearance of MEK2N, the quantification was done as follows. The cells were selected using the nuclei in the DAPI channel. Then, the cells were segmented using the CellTrace channel. To only quantify the cytoplasm, a mask for the cell was done excluding the nucleus. Finally, the median intensity of both MEK2N and CellTrace of each cell was calculated, and from that, the mean intensity of both MEK2N and CellTrace of all the cells in each well was computed. For each well, and therefore siRNA, both mean intensities were converted to 16bit. The MEK2N (0-1) and CellTrace (0.01-1) for each well were normalized per plate and the MEK2N value was divided by CellTrace to have a ratio of remaining MEK2. Finally, the Z-score was calculated of this ratio for each siRNA per plate. As there were duplicates in the screen, some later analyses used the average of the two Z-scores as the value for that well and siRNA. For the EEA1 screen, the images in the EEA1 channel were thresholded to remove the highest and lowest 0.05% pixels. The total perimeter of that channel was quantified, and then normalized by dividing by the square of the log base 10 of the cell number of each well. This value was then Z-score normalized per plate. As with the Toxin Entry screen, averages of the two Z-scores for the EEA1 screen were computed for later analyses. For both screens, a few siRNAs were removed that either were missing images or had less than 100 cells in their wells.

SDS-PAGE and western blots

Cells were normally lysed in immunoprecipitation buffer (IPB: 0.5% Nonidet P-40, 500 mM Tris pH 7.4, 20 mM EDTA, 10 mM NaF, 2 mM benzamidin, and protease inhibitor cocktail) and spun at 5,000 × g for 3 min to eliminate the DNA. Exceptionally, cells transfected with the PC-sensors were lysed in PBS supplemented with 1% Triton X-100, 1 mM EDTA, and 1 PI tab, and spun at 21,000 × g for 10 min. DNA-free lysates were quantified using Bicinchoninic acid (BCA) protein assay and denatured by addition of SDS sample buffer with β-mercaptoethanol and incubation for 5–10 min at 95 °C. Samples were migrated on precast Novex 4–20% or 4–12% polyacrylamide gels (Thermo Fisher Scientific), then transferred to Novex nitrocellulose membranes (Thermo Fisher Scientific) using iBlot 2. Blocking and antibody steps were performed using 5% milk in PBST (PBS with 0.5% Tween-20). Primary antibody steps were incubated overnight at 4 °C, while the membranes were incubated with secondary antibodies for 1 h at room temperature, both with gentle shaking. Three to five washes of PBST were performed before developing using the Fusion Solo-S (Viber-Smart Imaging) and the Fusion Solo chemiluminescence imaging system.

Anthrax toxin entry assays

Cells at 80–90% confluence were washed two times with minimal media Glasgow minimal essential media buffered with 10 mM HEPES at 4 °C and then incubated with toxin (anthrax toxin: 500 ng/mL PA and 50 ng/mL LF) for 30 min to 1 h at 4 °C. For cleaved (or pre-nicked) toxin, PA was incubated for 10 min with 100 μg/mL trypsin then stopped with 1 mg/mL of trypsin inhibitor for 1 min, and added to minimal media as for the uncleaved toxin. After the toxin incubation, cells were washed three times with minimal media and moved to 37 °C. The cells were lysed at the appropriate times shown in the experiments (0–2.5 h for experiments with anthrax toxin showing MEK cleavage; 0–90 min for experiments showing PA cleavage). For acid pulse treatment, lysates were treated with a 10% addition of isotonic buffer (145 mM NaCl, 20 mM MES-Tris pH 4.5) for 10 min at RT. Samples were run on gels as described above with GAPDH as loading controls. For comparison purposes, quantified values were normalized to time 0 (for MEK experiments)

or within each experiment (for PA experiments). The molecular weight of the SDS-resistant PA^{oligo} is not defined as it is above the top marker in SDS/PAGE. Experiments were repeated at least three times and representative blots are shown in the figures.

Cell surface protein pull-down

Surface biotinylation assays were performed as described previously (Sergeeva and van der Goot, 2019). Briefly, cells were shifted to ice and incubated for 30 min with cold biotinylation solution diluted in PBS (0.17-mg/mL final concentration), then quenched three times with cold 100 mM NH_4Cl. Cells were lysed as normally and about 5% of the DNA-cleared lysate was taken as a TCE control. The rest of the lysate was incubated with prewashed streptavidin-coupled beads (Sigma S1638) overnight at 4 °C. Finally, beads were washed and proteins were eluted from beads as above. GAPDH was used as an intracellular control. Experiments were repeated at least three times and representative blots are shown in the figures.

Lipid extraction

Total lipid extracts were prepared using a standard MTBE protocol for total lipid analysis by mass spectrometry. Briefly, cell pellet was resuspended in 100 μL H_2O. 360 μL methanol and 1.2 mL of MTBE were added and samples were placed for 10 min on a vortex at 4 °C followed by incubation for 1 h at room temperature on a shaker. Phase separation was induced by addition of 200 μL of H_2O. After 10 min at room temperature, samples were centrifuged at 1000x g for 10 min. The upper (organic) phase was transferred into a glass tube and the lower phase was re-extracted with 400 μL artificial upper phase [MTBE/methanol/H_2O (10:3:1.5, v/v/v)]. The combined organic phases were dried in a vacuum concentrator. The dried lipid pellet was then extracted using 300 μL water-saturated n-butanol and 150 μL H_2O. The organic phase was collected, and the aqueous phase was re-extracted twice with 300 μL water-saturated n-butanol. The organic phases were pooled and dried in a vacuum concentrator.

LC-MS untargeted lipidomics

The LC-MS analysis was performed using a Vanquish UHPLC system (Thermo Fisher Scientific) combined with an Orbitrap Fusion™ Lumos™ Tribrid™ mass spectrometer (Thermo Fisher Scientific). Lipid separation was performed by reversed phase chromatography employing an Accucore C18, 2.6 μm, 150 x 2 mm (Thermo Fisher Scientific) analytical column at a column temperature of 35 °C. As mobile phase A an acetonitrile/water (50/50, v/v) solution containing 10 mM ammonium formate and 0.1 % formic acid was used. Mobile phase B consisted of acetonitrile/isopropanol/water (10/88/2, v/v/v) containing 10 mM ammonium formate and 0.1% formic acid. The flow rate was set to 400 μL/min. A gradient of mobile phase B was applied to ensure optimal separation of the analysed lipid species. The mass spectrometer was operated in ESI-positive and -negative mode, capillary voltage 3500 V (positive) and 3000 V (negative), vaporize temperature 320 °C, ion transfer tube temperature 285 °C, sheath gas 60 arbitrary units, aux gas 20 arbitrary units and sweep gas 1 arbitrary unit. The Orbitrap MS scan mode at 120000 mass resolution was employed for lipid detection. The scan range was set to 250-1200 m/z for both positive and negative ionization mode, the AGC target was set to 2.0e5 and the intensity threshold to 5.0e3. The data analysis was performed using the TraceFinder software (ThermoFisher Scientific).

Sphingosine pulse and chase

RPE1 cells were pulse-labelled in serum-free 2% fatty-acid-free BSA in DMEM, at a final concentration of 1 μCi/mL [3H]-sphingosine, for 2 h. Cells were chased in complete medium for the indicated times, harvested and processed for lipid extraction. Lipids were spotted onto silica-gel high performance-TLC (HPTLC) plates (Merck, Germany) (Capasso et al., 2017), and resolved with a mixture of chloroform: methanol: water (65:25:4 v/v/v). To visualise the unlabelled standards (i.e., Cer, GlcCer, LacCer, Gb3, SM and GM3) the TLC plates were placed in a sealed tank saturated with iodine vapour, while the radiolabelled lipids were analysed using a RITA® TLC Analyser (Raytest, Germany), and quantified using GINA® (Raytest, Germany) software analysis.

Detergent resistant membrane (DRMs)

DRMs were prepared from RPE1 cells as described previously using OptiPrep (Alere Technologies #1114542) gradients as previously published (Abrami et al., 2003; Sergeeva and van der Goot, 2019). Briefly, cells were lysed on ice in TNE buffer (25 mM TrisHCl, pH 7.4; 150 mM NaCl; 5 mM EDTA) supplemented with 1% Triton X-100 and applied to the bottom of a gradient consisting of three layers: 60% OptiPrep with sample, 30% OptiPrep in TNE and 50% TNE. After a 2-h run at 55,000 rpm in a Thermo Fisher Scientific S55-S rotor, six equal fractions were carefully collected from the top. Fractions were run on SDS/PAGE for western blots or used for mass spectrometry. Experiments were repeated at least three times and representative blots are shown in the figures.

Mass spectrometry

SDS-PAGE gel slices were washed twice in 50% ethanol and 50 mM ammonium bicarbonate for 20 min and dried by vacuum centrifugation. Samples reduction was performed with 10 mM dithioerythritol for 1 h at 56 °C. A washing-drying step as described above was repeated before performing sample alkylation with 55 mM Iodoacetamide for 45 min at 37 °C in the dark. Samples were washed-dried again and digested overnight at 37 °C using Mass Spectrometry grade trypsin at a concentration of 12.5 ng/μL in 50 mM ammonium bicarbonate and 10 mM calcium chloride. Resulting peptides were extracted in 70% ethanol, 5% formic acid twice for 20 min with permanent shaking. Samples were further dried by vacuum centrifugation and stored at -20 °C. Peptides were desalted on SDB-RPS StageTips (Rappsilber et al., 2007) and dried by vacuum centrifugation. For TMT labelling, peptides were first reconstituted in

8 μL HEPES 100 mM (pH 8.5) containing 10 ng trypsin-digested Chicken Ovalbumin. Labeling was performed by adding 3 μL of TMT solution (20 μg/μL in pure acetonitrile) and incubating samples at room temperature for 1.5 h. Reactions were quenched with hydroxylamine to a final concentration of 0.4% (v/v) for 15 min. TMT-labelled samples were then pooled at a 1:1 ratio across all samples and dried by vacuum centrifugation. Samples were then fractionated into 12 fractions using an Agilent OFF-GEL 3100 system. Resulting fractions were desalted on SDB-RPS StageTips and dried by vacuum centrifugation. Each individual fraction was resuspended in 10 μL of 2% acetonitrile, 0.1% formic acid and nano-flow separations were performed on a Dionex Ultimate 3000 RSLC nano UPLC system on-line connected with a Lumos Fusion Orbitrap Mass Spectrometer. A capillary precolumn (Acclaim Pepmap C18, 3 μm-100 Å, 2 cm x 75 μm ID) was used for sample trapping and cleaning. Analytical separations were performed at 250 nL/min over 150 min. biphasic gradient on a 50cm long in-house packed capillary column (75μm ID; ReproSil-Pur C18-AQ 1.9μm; Dr. Maisch). Acquisitions were performed through Top Speed Data-Dependent acquisition mode using a 3 seconds cycle time. First MS scans were acquired at a resolution of 120,000 (at 200 m/z) and the most intense parent ions were selected and fragmented by High energy Collision Dissociation (HCD) with a Normalized Collision Energy (NCE) of 37.5% using an isolation window of 0.7 m/z. Fragmented ions were acquired with a resolution 50,000 (at 200 m/z) and selected ions were then excluded for the following 120 s.

Raw data were processed using SEQUEST, Mascot, MS Amanda (Dorfer et al., 2014) and MS Fragger (Kong et al., 2017) in Proteome Discoverer v.2.4 against a concatenated database consisting of the Uniprot Human Reference Proteome (Uniprot Release: 2019_06) and common contaminants including chicken Ovalbumin (Uniprot Accession Number: P01012). Enzyme specificity was set to Trypsin and a minimum of six amino acids was required for peptide identification. Up to two missed cleavages were allowed. A 1% FDR cut-off was applied both at peptide and protein identification levels. For the database search, carbamidomethylation (C), TMT tags (K and Peptide N termini) were set as fixed modifications, while oxidation (M) was considered as a variable one. Resulting text files were processed through in-house written R scripts (version 3.6.3) (Schindelin et al., 2012). The unnormalized abundances calculated by Proteome Discoverer were transformed in $\log_2$ and subtracted to obtain ratios. The Z-scores of the ratio of ratios [F2 (siTMED2/10/siCtl) / Input (siTMED2/10/siCtl)] were calculated.

Immunofluorescence

HeLa or RPE1 cells were plated at about 50% confluency after transfection. Cells were washed with PBS, fixed in 4% paraformaldehyde (PFA), washed thoroughly with PBS, quenched with 50 mM NH_4Cl, and washed again with PBS. When applicable, cells were permeabilized with 0.1% Triton X-100 in PBS for 5 min. After, cells were washed and blocked with 1% BSA in PBS. Primary and secondary antibody incubations were done in the same buffer. Where applicable, D4-mCherry at 9.5 μg/mL was applied for 1 h; Filipin III at 50 μg/mL for 15 min. Finally, coverslips were mounted in Prolong Glass Antifade Mountant. Images were acquired using either confocal LSM710 (Carl Zeiss AG) or Leica-SP8 (Leica Biosystems) with 63X objective and a pinhole size of 1 AU and at least 2 line-averaging. Images were processed using Fiji ImageJ (Schindelin et al., 2012).

Lysenin staining

Cells were starved in FBS freμe medium for overnight before incubation with Lysenin-GFP for 30 min at 4° C. Cells were then fixed in PFA for 10 min and imaged as explained above.

PtdIns(4)P staining

Cells were quenched with 50 mM NH_4Cl and fixed in 2 % PFA for 15 min and permeabilized with 2 μM digitonin in buffer A (20 mM PIPES pH 6.68, 135 mM NaCl and 27 mM KCl). Cells were then blocked with 5 % FBS in buffer A and stained with mouse anti-PtdIns(4)P in the same solution. After secondary antibody staining, cells were fixed again in with 2 % PFA for 10 min. Cells were then washed with PBS and imaged as above.

Automated fluorescence microscopy and quantification

Cells were plated at $2x10^4$ cells per well and silenced for 72h with either siCtl and siTMED2/10 following manufacturer's instructions in Ibidi 96-well μplates. Cells were fixed with 3% PFA and permeabilized with 0.05% saponin. Cells were then stained with primary antibodies followed by incubation with (when required) secondary antibodies tagged with alexa-fluor (488 or 568) with Hoechst. Images were acquired with either 40X or 60X plan Apo.

MetaXpress Custom Module editor software from Molecular Devices was used to extract different parameters such as signal intensity or objects, as in previous publications (Larios et al., 2020; Moreau et al., 2019). Cell mask was created using Hoechst to create the master object (cell). Golgi was segmented using either GM130 or GOLPH3. These masks were then applied on the fluorescent images to extract relevant measurements. When indicated, a perinuclear mask (4-μm-diameter region immediately outside the nucleus) to quantify cholesterol (filipin) signals inside and outside this perinuclear area was used. The final masks were applied to all original fluorescent images and measurements per cell and averages per well were extracted. For GM130-positive objects, all objects per cell were analysed. The same analysis pipeline was applied to all images.

BrdU staining and flow cytometry assay

Control and silenced RPE1 cells were stained using FITC BrdU Flow Kit at 50% confluency. Briefly, cells were treated (or not for unstained control) with 10 μl BrdU per 1 mL of the medium for 45 min at 37 °C. Cells were then washed, trypsinised and fixed in 100 μL of

BD Cytofix/Cytoperm buffer for 20 min at RT, washed with BD Perm/Wash buffer and permeabilized in 100μl of BD Cytoperm Permeabilization Buffer Plus and incubated for 10 min on ice. After washing, cells were fixed again in BD Cytofix/Cytoperm buffer for 5 min at RT, washed, resuspended in 100 ul DNAse solution for 60 min at 37 °C and washed again. Cells were then stained with 50 μL anti-BrdU antibody for 20 min at RT followed by washing. Finally, cells were resuspended in 20 μL 7-AAD solution for 5 min. All washing steps were performed using BD Perm/Wash buffer. Cells were diluted in 1 mL PBS and analyzed using BD LSR II SORP. BrdU was excited at 488 nm and emission was collected at 525 ± 50 nm. 7-AAD was excited with 561 nm laser and 660 ± 20 nm emission filter was used. A total of 50,000 events were collected per condition. Data were analyzed using FlowJo v10.

In situ proximity ligation assay

In situ proximity ligation (PLA) assay were performed using materials and guidelines provided with DuoLink PLA kit. Briefly, cells were fixed and permeabilized as mentioned above. Cells were blocked in DuoLink blocking solution and incubated with rabbit anti-OSBP and mouse anti-VAPA antibodies. Cells were next incubated with anti-mouse PLUS and anti-rabbit MINUS secondary probes followed by ligation and amplification with specific reagents. Cells were imaged using a laser-scanning-confocal microscope. Images were processed using Fiji ImageJ and PLA spots were quantified using TrackMate (Schindelin et al., 2012).

Quantitative real-time PCR

RNA was extracted from RPE1 cells using the Qiagen RNAeasy kit and QIAshredder. RNA concentration was measured and 500 ng of total RNA was used for cDNA synthesis using iScript. A 1:5 dilution of cDNA was used to perform quantitative real-time PCR using Applied Biosystems SYBR Green Master Mix on 7900 HT Fast QPCR System (Applied Biosystems) or QuantStudio 6 Pro Real-Time PCR System (Thermo Fisher Scientific) with SDS 2.4 Software. Primers (see Table S4 for sequences) were validated with standard curves over 4 dilutions. The data (always in triplicate) were normalized using multiple housekeeping genes. For real-time quantitative PCR, data was processed using R (R Core Team, 2019).

RNA sequencing

RNA quality was controlled on the TapeStation 4200 (Agilent), confirming that all were of good quality (scores >9.6). Libraries for mRNA-seq were prepared with the Stranded mRNA Ligation method (Illumina) starting from 1ug RNA, according to manufacturer's instructions. Libraries, all bearing unique dual indexes, were subsequently loaded at 1.44 pM on a NextSeq 500 high output flow cell (Illumina) and sequenced according to manufacturer instructions, yielding pairs of 80 nucleotides reads. Reads were trimmed of their adapters with bcl2fastq v2.20 (Illumina) and quality-controlled with fastQC v0.11.9.

Paired-end sequencing reads were aligned using STAR (version 2.7.9a) to the Human reference genome GRCh38 (gencode v36, Ensembl 102). Quantification of uniquely mapped reads to the genes was performed with HTSeq counts (Part of the 'HTSeq' framework, version 0.12.4) with the following parameters *-s reverse -m intersection-nonempty -r pos -t exon -i gene_id -q*. Counts pre-processing and differential analysis was done in R (version 4.0), using edgeR (v. 3.30.3) and DESeq2 package (v. 1.28.1) (Robinson et al., 2010). A total of 11'995 protein-coding genes with a cpm value greater than 1 in at least 2 samples were considered for the rest of the analysis.

Coimmunoprecipitations

Coimmunoprecipitations were performed as described previously (Bürgi et al., 2020; Sergeeva and van der Goot, 2019). Briefly, RPE1 or HeLa cells were lysed normally as described above. A tenth of the lysate was taken as TCE control and the rest was added to washed Protein G-coupled Sepharose beads for preclearing (30 min). The lysates were then added to freshly washed Protein G beads containing antibody for an overnight incubation at 4 °C. Proteins were eluted off the beads and divided for Western blots for direct immunoprecipitation and coimmunoprecipitation. Experiments were repeated at least three times and representative blots are shown in the figures.

Retention using selective hooks

Control and silenced cells were transfected with plasmid encoding for streptavidin-KDEL hook and streptavidin binding peptide (SBP)-EGFP-GPI for 24 h prior to imaging. To release the cargo from the ER-hook, 40 μM D-Biotin containing media was introduced (Boncompain et al., 2012). Cells were imaged live at 60 sec intervals for 45 min using Visitron Spinning Disk confocal microscope (Visitron).

Alkaline phosphatase activity assay

Alkaline phosphatase activity was determined using Alkaline Phosphatase Assay Kit (Abcam) according to manufacturer's protocol. Briefly, control and silenced cells were transfected with pSEAP2-secALP plasmid for 24 h. Media was collected at 0 h, 1 h, 2 h and 3 h timepoints. 80 μL of sample was incubated with 50 μL of 5 mM p-Nitrophenyl Phosphate (pNPP) solution for 60 min at RT. In parallel, fresh standards of 0-20 μmol pNPP were treated with 10 ul of ALP enzyme. The reaction was stopped by adding 20 μL stop solution. Samples were analyzed for absorbance at 405 nm to determine the levels of dephosphorylated product p-Nitrophenyl (pNP). Values were calculated based on the standard curve and were normalized to zero for the time point 0 h.

Live/dead cell count

After 72 h of transfection, siCtl or siTMED2/10 cells were trypsinized and counted for further 72 h at 24 h intervals using Countess-cell-counter (Life technologies). Trypan Blue was used to calculate live/dead ratio.

QUANTIFICATION AND STATISTICAL ANALYSIS

Western blot quantifications were done using Fiji (Schindelin et al., 2012). Figures were generated and statistics were performed as described in the figure legends using GraphPad Prism or R statistical computing environment (R Core Team, 2019). Throughout the study, indicated significance asterisks are as follows: *$P < 0.05$, **$P < 0.01$, ***$P < 0.001$ and ****$P < 0.0001$, while unmarked comparisons with control are not significant. All error bars are SEMs. For all areas under curve (AUC) t-testing compared with the control, specific P values are reported on each graph. The pathway analysis figure was made using the ClueGo application of Cytoscape v3.7 (Bindea et al., 2013).